J. Fluid Mech. (2018), *vol.* 837, *pp.* 48–79. © Cambridge University Press 2017
doi:10.1017/jfm.2017.835

The regular reflection→Mach reflection transition in unsteady flow over convex surfaces

M. Geva[1], O. Ram[1] and O. Sadot[1,†]

[1]Pearlstone Center for Aeronautical Engineering Studies, Department of Mechanical Engineering, Faculty of Engineering Sciences, Ben-Gurion University of the Negev, Beer Sheva, 84105, Israel

(Received 3 June 2016; revised 29 October 2017; accepted 14 November 2017; first published online 19 December 2017)

The non-stationary transition from regular reflection (RR) to Mach reflection (MR) over convex segments has been the focus of many recent studies. Until recently, the problem was thought to be very complicated because it was believed that many parameters such as the radius of curvature, initial angle and geometrical shape of the reflecting surface influenced this process. In this study, experiments and inviscid numerical computations were performed in air ($\gamma = 1.4$) at an incident shock-wave Mach number of 1.3. The incident shock waves were reflected over cylindrical and elliptical convex surfaces. The computations were validated by high-resolution experiments, which enabled the detection of features in the flow having characteristic lengths as small as 0.06 mm. Therefore, the RR→MR transition and Mach stem growth were successfully validated in the early stages of the Mach stem formation and closer to the surface than ever before. The evolution of the RR, the transition to MR and the Mach stem growth were found to depend only on the radius of the reflecting surface. The reflected shock wave adjusts itself to the changing angles of the reflecting surface. This feature, which was demonstrated at Mach numbers 1.3 and 1.5, distinguishes the unsteady case from the self-similar pseudo-steady case and requires the formulation of the conservation equations. A modification of the standard two-shock theory (2ST) is presented to predict the flow properties behind a shock wave that propagates over convex surfaces. Until recently, the determination of the time-dependent flow properties was possible solely by numerical computations. Moreover, this derivation explains the controversial issue on the delay in the transition from the RR to the MR that was observed by many researchers. It turns out that the entire RR evolution and the particular moment of transition to MR, are based on the essential 'no-penetration' condition of the flow. Therefore, we proposed a simple geometrical criterion for the RR→MR transition.

Key words: compressible flows, shock waves

1. Introduction

The proper prediction of reflection configurations is crucial in many engineering applications, e.g. shock-wave focusing, supersonic flights and protection against blasts. While the criterion for non-stationary transitions is in dispute, the criterion for the

† Email address for correspondence: sorens@bgu.ac.il

https://doi.org/10.1017/jfm.2017.835 Published online by Cambridge University Press

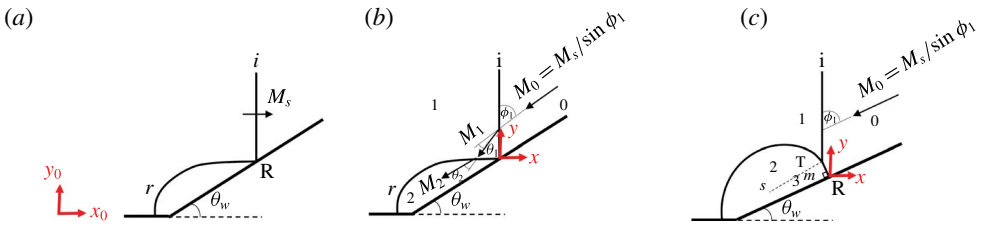


FIGURE 1. (Colour online) Schematic illustrations of a reflection over a wedge. (*a*) Regular reflection in a laboratory reference frame; (*b*) regular reflection in a reference frame attached to the reflection point; and (*c*) Mach reflection in a reference frame attached to the reflection point.

transitions from regular reflection (RR) to Mach reflection (MR) in pseudo-steady and steady flow reflections is well established (Ben-Dor 2007). The reflection configuration in pseudo-steady flows forms when a plane shock wave propagates at a constant Mach number M_s and interacts with a plane surface inclined at an angle θ_w. The orientation of the waves in this scenario remains constant throughout the incident shock propagation along the surface. Hence, the boundary condition does not change. The reflection is a regular reflection when θ_w is higher than a certain value. Figure 1(*a*,*b*) depicts an RR configuration comprising the incident shock, *i*, and the reflected shock, *r*, both intersecting at the reflection point, R.

The analytical treatment of pseudo-steady flows usually requires the use of a Galilean transformation, such that the flow passing through the shock can be considered steady. The transformation is performed by moving the laboratory reference frame (figure 1*a*) to a frame attached to the reflection point (figure 1*b*). Both frames differ only by a constant relative motion $M_0 = M_s/\sin(\phi_1)$ along the surface. The RR configuration can be analytically solved using the standard two-shock theory (2ST) developed by von Neumann (1943*a*). This theory solves the conservation equations of both shock waves under the geometrical restrain that dictates an equality of the deflection angles, $\theta_1 = \theta_2$ (figure 1*b*). The MR consists of a three shock waves configuration (i.e. *i*, *r* and a Mach stem *m*) intersecting at the triple point, T (figure 1*c*). The analytical solution of the three-shock theory (3ST) was developed by von Neumann (1943*b*).

von Neumann (1943*a*) argued that the RR↔MR transition depends on whether the corner-generated signals, emanating from the wedge corner, can catch up with the reflection point. Later, Hornung, Oertel & Sandeman (1979) introduced the length scale criterion. This criterion is based on the assumption that an MR, which includes a finite length of the Mach stem, must be related to a finite length scale. In pseudo-steady flows, this length is the distance between the corner and reflection point. Hence, for the RR to communicate with the corner, the flow behind the reflection point must be subsonic. This criterion is also known as the 'sonic criterion', which is very close to the 'detachment criterion' (the maximum deflection point, θ_m, is very close to the sonic point, θ_s). The termination of the RR can be calculated using the 2ST while constraining the deflection angle behind the reflected shock, θ_2, to be $\theta_2 = \theta_{2m}$ or $\theta_2 = \theta_{2s}$ (figure 1*b*). Although the conditions are practically similar (Ben-Dor 2007), Lock & Dewey (1989) experimentally showed that in pseudo-steady flows, transitions occur at the sonic criterion, where the corner-generated signals can catch up with the reflection point. However, readers should note that this delicate observation was made based on experiments having certain resolution limits that were

https://doi.org/10.1017/jfm.2017.835 Published online by Cambridge University Press

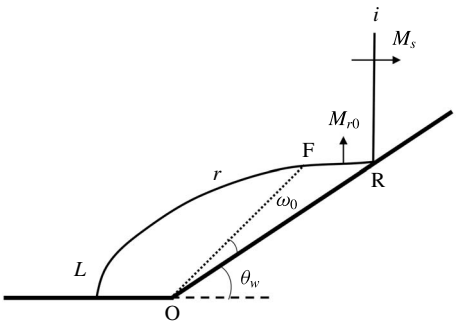


FIGURE 2. Schematic description of the interaction between a signal originating from the corner, OF, and the reflected shock wave over a wedge (Han 1991).

common 30 years ago. Hence, the reliability of accurately identifying the exact sonic point is uncertain. Han (1991) applied modified shock dynamic relations, originally developed by Whitham (1968), to pseudo-steady reflections in which a uniform flow exists ahead of the shock wave. He was able to describe the mechanism through which the reflected shock is disturbed and curved by sound waves emanating from the corner (figure 2). The incident and reflected shock waves travel at M_s and M_{r0}, respectively. The first sound wave originating from the corner, O, interacts with the reflected shock and forms the first disturbance point, F. The part of the reflected shock between R and F is straight and is not affected by the surface. Beyond this point, the shock becomes curved. Evaluating the reflected shock strength and orientation in this section is possible using the shock dynamic theory. Although Han's modification is useful, further improvements are still needed (Han & Yin 1993). The RR→MR transition, according to this method, is acquired when the first disturbance originating from the corner reaches the reflection point, R.

The unsteady shock-wave reflection over convex surfaces is far more complicated than steady and pseudo-steady reflections. The complications arise because a continuous change in the surface angle introduces a continuous change of the boundary conditions. The flow Mach number, M_0, and its orientation, ϕ_1, are continually changing. In the convex plane case, the reflection begins as an RR (figure 3*a*). The reflection then transforms into an MR as the surface wedge angle decreases and the RR configuration can no longer deflect the flow (figure 3*b*). Takayama & Sasaki (1983) performed an extensive set of experiments in order to investigate the RR→MR transitions over convex cylindrical models. They found that the curvature radii, initial angles and incident shock-wave strengths affect the transition. The RR→MR transition occurs at smaller angles than those predicted by the known criteria both in steady and pseudo-steady flows. Similar trends were observed by Skews & Kleine (2009, 2010) and Skews & Blitterswijk (2011) which utilised the perturbation technique. Yet, as the radii increases, the transition approaches the known pseudo-steady criterion (Ben-Dor 2007). Several analytical attempts were made to model the complexity of the transition process.

Bryson & Gross (1961) applied the shock dynamic theory to the shock wave diffraction by a cylinder. They found an analytical solution that describes the growth of the Mach stem in an MR. Heilig (1969) utilised the shock dynamic theory to form an RR→MR transition criterion. Later on, Itoh, Okazaki & Itaya (1981) adjusted Heilig's criterion by considering Milton's (1975) modifications. Li (1988) used

https://doi.org/10.1017/jfm.2017.835 Published online by Cambridge University Press

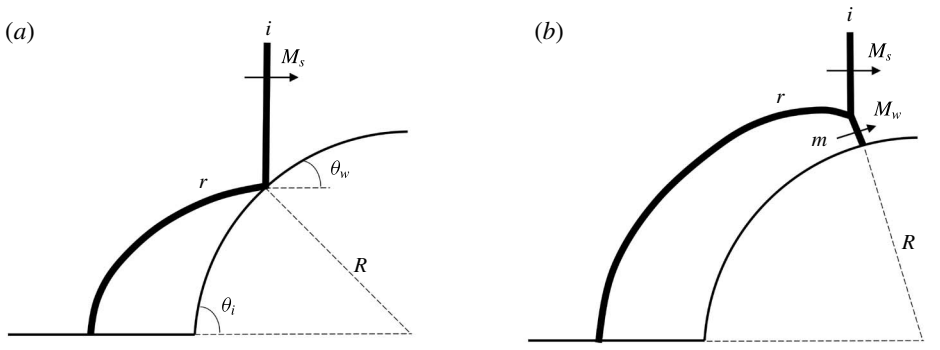


FIGURE 3. Illustration of the reflection configurations over a convex circular cylindrical surface having an initial angle θ_i and a radius R: (*a*) RR, which consists of an incident shock wave, *i*, and a reflected shock wave, *r*, and (*b*) MR, which consists of an incident shock wave, *i*, a reflected shock wave, *r*, and a Mach stem, *m*.

the concept of disturbance propagation to obtain an RR→MR transition criterion. Unfortunately, the proposed criteria that were mentioned above did not consider the effect of the radius of curvature on the transition (Han & Yin 1993). Furthermore, these criteria did not agree with the RR→MR transition recorded in any of the high-resolution numerical and experimental studies (Kleine *et al.* 2014; Ram, Geva & Sadot 2015).

Several recent studies claimed that the inconsistency between the unsteady and the pseudo-steady measured transition angles simply arises from an insufficient optical resolution. Thus, the transition criterion is the same as that in the pseudo-steady case (Timofeev *et al.* 1999; Hakkaki-Fard & Timofeev 2012; Kleine *et al.* 2014). In the high-resolution computational study by Hakkaki-Fard & Timofeev (2012), only a small deviation was found between the RR→MR transition and sonic criterion. Their results were obtained for a single unspecified radius of curvature and single initial angle. The reflection was deemed as an MR if at least one grid cell had a subsonic speed in the reference frame attached to the reflection point. To compute this condition, three equivalent methods were demonstrated. Kleine *et al.* (2014) discussed the problematic detection of the transition. Many studies determined the transition at the moment in which the Mach stem is first observed. Since it is easier to resolve a Mach stem when larger radii are involved, the transition seems to approach the pseudo-steady criterion. However, if a proper experimental set-up that resolves 0.05 mm is used, the radii dimension should not affect the transition. Ram *et al.* (2015) experimentally investigated the RR→MR transition at high spatial and temporal resolutions. Their experimental set-up could realise, for the first time, the desirable spatial resolution suggested by Kleine *et al.* (2014). In this study, they also addressed the problematic detection of the transition angle from the trajectory of the triple point and showed that a clear difference exists between the detachment criterion and actual transition in the experiments. Among the researchers who study transient shock reflections, there is still a major debate concerning the proper RR→MR criterion and the accurate method to detect the transition.

In the present study, high-resolution numerical computations were validated using high-resolution spatial experiments. The tested convex models had varying radii, initial angles and surface change rates. In the following sections of this paper, we show that the RR evolution, the transition to MR and the Mach stem growth rate depend on

https://doi.org/10.1017/jfm.2017.835 Published online by Cambridge University Press

a single geometrical scale, i.e. the radius of curvature. We present a modification of the standard 2ST to suit the unsteady reflections. The modified 2ST solution is then compared with validated numerical computations. We provide a physical explanation to the inconsistency between the pseudo-steady and unsteady reflections, including the possible reason for the delay in the RR→MR transition. Finally, we suggest a new simple geometrical criterion for the transition based on the 'no penetration' of the flow condition.

To the best of the authors' knowledge, this is the first study to present a solution that resolves the flow conditions around an unsteady shock-wave reflection and this is the first time that all the parameters suggested by Takayama & Sasaki (1983) are tested by numerical and experimental means.

2. Methodology

2.1. *Numerical simulations*

Computations were carried out using a commercial computational fluid dynamics solver (Fluent, ANSYS® Academic Research, Release 15.0), which employed a control-volume-based technique. The program solved the inviscid Euler equations approximated with second-order (space and time) schemes. The spatial discretisation of the convection and diffusion terms was evaluated using a second-order upwinding total variation diminishing method that employed the Barth–Jespersen minmod limiter (Barth & Jespresen 1989). Gradients in the upstream cell were calculated by the Green–Gauss node-based gradient evaluation (Holmes & Connell 1989; Rausch, Batina & Yang 1992). Transient terms in the differential equations were calculated by second-order explicit time-stepping integration based on a four-stage Runge–Kutta method (Jameson, Schmidt & Turkel 1981). A structured grid was refined at several levels. Thus, the results presented in this paper are grid independent. Since a commercial software was used, extra caution was taken during the experimental validation of the results.

2.2. *Experiments*

The experiments were performed using a fully automated experimental apparatus located at the shock tube laboratory in the Mechanical Engineering Department, Faculty of Engineering Sciences of the Ben-Gurion University of the Negev. The entire operation of the vertical shock tube together with single-frame schlieren image-capturing system was computer controlled. The shock tube consists of a 4.5 m driven section having a square cross-section of 80×80 mm and a 2 m driver section having a 90 mm circular section. The driver and driven sections are separated by a fast opening valve (KB-40A, ISTA Inc.). The incident shock-wave Mach number was measured using two piezoresistive pressure transducers (8530B-500, Endevco), which were installed 600 mm apart. In each experiment, a single 16.2 Megapixel frame was captured by a digital SLR camera (D7000, Nikon). The spatial resolution provided a pixel size of 0.03 mm, which facilitated the tracing of features in the flow with characteristic sizes of 0.06 mm. The temporal resolution obtained was 1–2 μs. More details on the experimental set-up can be found in Geva, Ram & Sadot (2013) and Ram *et al.* (2015).

2.3. *Image-processing procedure*

Both the numerical and experimental results were analysed using the same in-house user-independent image-processing procedure, which is described in detail by Geva

https://doi.org/10.1017/jfm.2017.835 Published online by Cambridge University Press

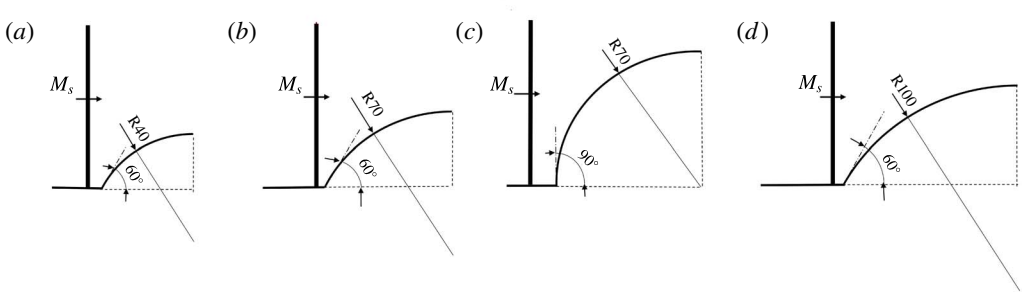


FIGURE 4. Dimension specifications of the circular–cylindrical convex models: (*a*) $R = 40$ mm, $\theta_i = 60°$; (*b*) $R = 70$ mm, $\theta_i = 60°$; (*c*) $R = 70$ mm, $\theta_i = 90°$; and (*d*) $R = 100$ mm, $\theta_i = 60°$.

et al. (2013). In each frame, the procedure located the triple point and the reflection point automatically. The reflection point was found to be the intersection of the Mach stem and surface. Then, the length of the Mach stem and the surface angle were computed. The major advantage of this procedure is the elimination of selective interpretations that are sensitive to optical distortions and resolution limitations. A discussion on obtaining the error estimation when using this method can be found in Ram *et al.* (2015).

3. Results and discussion

3.1. *Validation of the numerical computations*

The investigation of the RR→MR transitions was initially performed using four circular–cylindrical convex reflecting surfaces having different radii and initial angles (figure 4). The different radii were 40, 70 and 100 mm, and the initial angles varied between 60 and 90°. Numerical computations were carried out for models (*a–d*) at an incident shock-wave Mach number of 1.3. Experimental validations were executed for models (*b–d*) which account for changes in curvature and initial angle. When the reflection occurs over a cylindrical surface, the rate of change is held constant during the process. However, to the best of the authors' knowledge, the evolution of RR and the transition to MR has not been analysed under a varying rate of change. To analyse this effect, two elliptical convex models were examined numerically. The dimensions of the models are shown in figure 5. As the reflection advances downstream (figure 5*a*), the radius of curvature of the ellipse increases and the rate of change decreases. However, the ellipse in figure 5(*b*) exhibits the opposite behaviour. Figure 6 shows the successive reflection process over cylindrical model (*d*) having a radius of 100 mm. Figure 6(*a*,*b*) shows the experimental results, whereas figure 6(*c*,*d*) is obtained by the simulations. The incident shock wave travels from left to right. In the early stages, the reflection is an RR (figure 6*a*,*c*). As the shock continue to propagate, the transition to MR occurs (figure 6*b*,*d*). As can be seen, the simulation results are in excellent agreement with the experimental results in terms of the shape of the reflection.

However, further analysis is required near the reflection point so that the reflection type can be accurately assessed (squares in figure 6). Therefore, images from both the simulations and the experiments were analysed using the image-processing program. The reflection was classified as an MR or an RR according to the calculated length

https://doi.org/10.1017/jfm.2017.835 Published online by Cambridge University Press

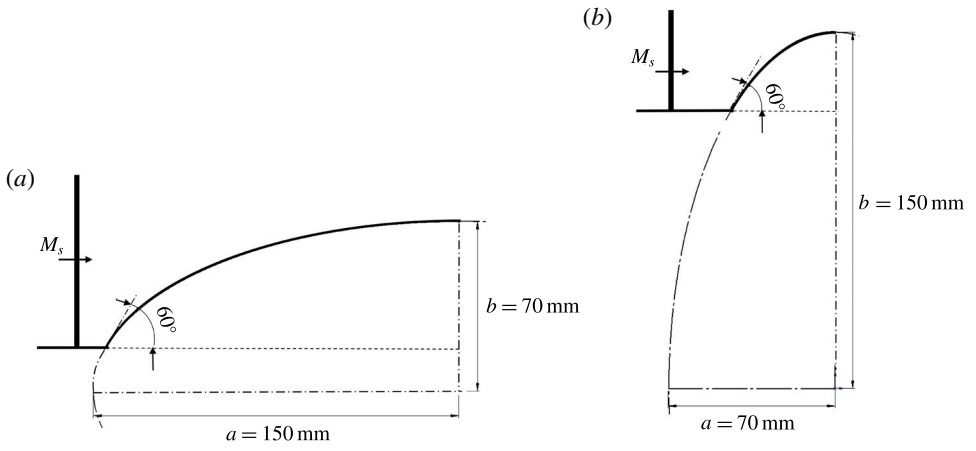


FIGURE 5. Dimensions of the elliptical models: (*a*) ellipse with an increasing radius of curvature and (*b*) ellipse with a decreasing radius of curvature.

of the Mach stem. If the Mach stem length was zero or larger, the reflection was classified as an MR or RR, respectively. The results of the procedure can be seen in figure 7. In figure 7(*a*,*c*), the program identified an RR, and in figure 7(*b*,*d*), it identified an MR having a Mach stem length of approximately 0.8 mm. A noticeable difference between the experiments and simulations was in the shock-wave width; in the experiments, the shock appeared to be more dispersed. Because the program locates the centre of the shock waves, it may yield a slight deviation between the triple points identified by the procedure and its real location. The lengths of the Mach stem and the related reflecting surface angle were obtained from the entire numerical and experimental results and are plotted in figure 8. In this figure, the validation for models (*b–d*) is shown. To account for the possible error in the evaluation of the Mach stem length caused by the shock width, ± 5 pixel limiters were added, which are 65 times the standard deviation of the experimental results. The simulation results were compared to hundreds of experimental images and showed great agreement with the experimental results for the entire reflection process. Owing to the high spatial resolution of the experimental set-up, the numerical computations were validated in the early stages of the Mach stem formation. To the best of the authors' knowledge, no numerical computations have so far been validated below 1.5 mm. Thus, any previous attempts to describe the behaviour at these minuscule lengths, measured so close to the reflecting surface, cannot be considered as validated. Being rigorously validated, the numerical simulation used in the following sections can be considered comparable to using experimental results.

3.2. *The evolution of an RR over a convex surface*

The analogy between pseudo-steady and unsteady reflections in terms of the RR evolution and RR→MR transition is simply inadequate as was performed by previous studies (Hakkaki-Fard & Timofeev 2012; Vignati & Guardone 2016). Since the physical behaviours of these flows are different, they cannot be described by the same theoretical method. Figure 9 demonstrates this fundamental difference between pseudo-steady and unsteady reflections. It is shown that pseudo-steady reflections are self-similar and can be scaled by the distance from the edge of the surface to the

https://doi.org/10.1017/jfm.2017.835 Published online by Cambridge University Press

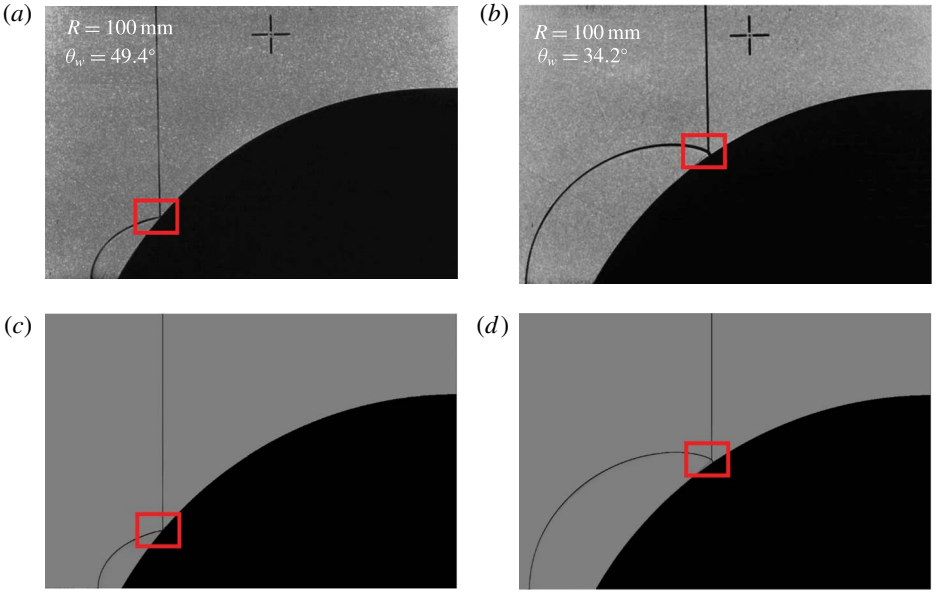


FIGURE 6. (Colour online) Schlieren images from the experiment (*a*,*b*) and simulation (*c*,*d*) for the 100 mm model at $M_s = 1.3$. (*a*,*c*) RRs at $\theta_w = 49.4°$, (*b*,*d*) MRs at $\theta_w = 34.2°$.

reflection point, R (figure 9*a*). Although, the wave configuration grows in time the orientations of the waves remains the same. Resulting in the same thermodynamic properties behind the reflected shock wave. This is in contrast with the unsteady reflection shown in figure 9(*b*). The reflected shock wave adjusts itself to the changing angles of the reflecting surface. Therefore, its orientation with respect to the incident shock wave changes as well. The reflection evolution in the unsteady case is definitely not self-similar and cannot be compared with the pseudo-steady reflections as will be shown in the next sections.

The change in the reflected shock-wave orientation during the reflection process over the 40 mm cylindrical model is demonstrated in figure 10. This figure shows the full frames from the computations (*a–c*) and the magnification of the reflection area in (*d–f*). The inclination angles of a straight small section of the reflected shock waves, α, were measured with respect to the incident shock direction. The angles were found through an automatic image-processing routine and are marked in the magnified images (figure 10*d–f*). It is shown that the measured angles, α, decrease as the surface angle continues to decrease. In non-stationary reflections the reflected shock wave is continually communicating with the surface (Skews & Kleine 2010) where 'signals' emerge from the surface and influence the reflected wave.

In contrast to the non-stationary flows, in the case of pseudo-steady flow, the corner is the only origin of disturbances communicating with the curved part of the reflected shock wave. This distinction has a major influence not only on the inter-shock-waves angle but also on the resulting thermodynamic properties near the reflection point. Figure 11 compares the reflection configurations obtained at a straight wedge with reflections obtained over the 40, 70 and 100 mm models at the same surface angle. In (*a–d*), the magnified schlieren images and the reflected shock wave orientation as was found automatically by the image-processing procedure are plotted. In pseudo-steady flows (figure 11*a*), the two-shock theory predicts a 90° angle between the incident

https://doi.org/10.1017/jfm.2017.835 Published online by Cambridge University Press

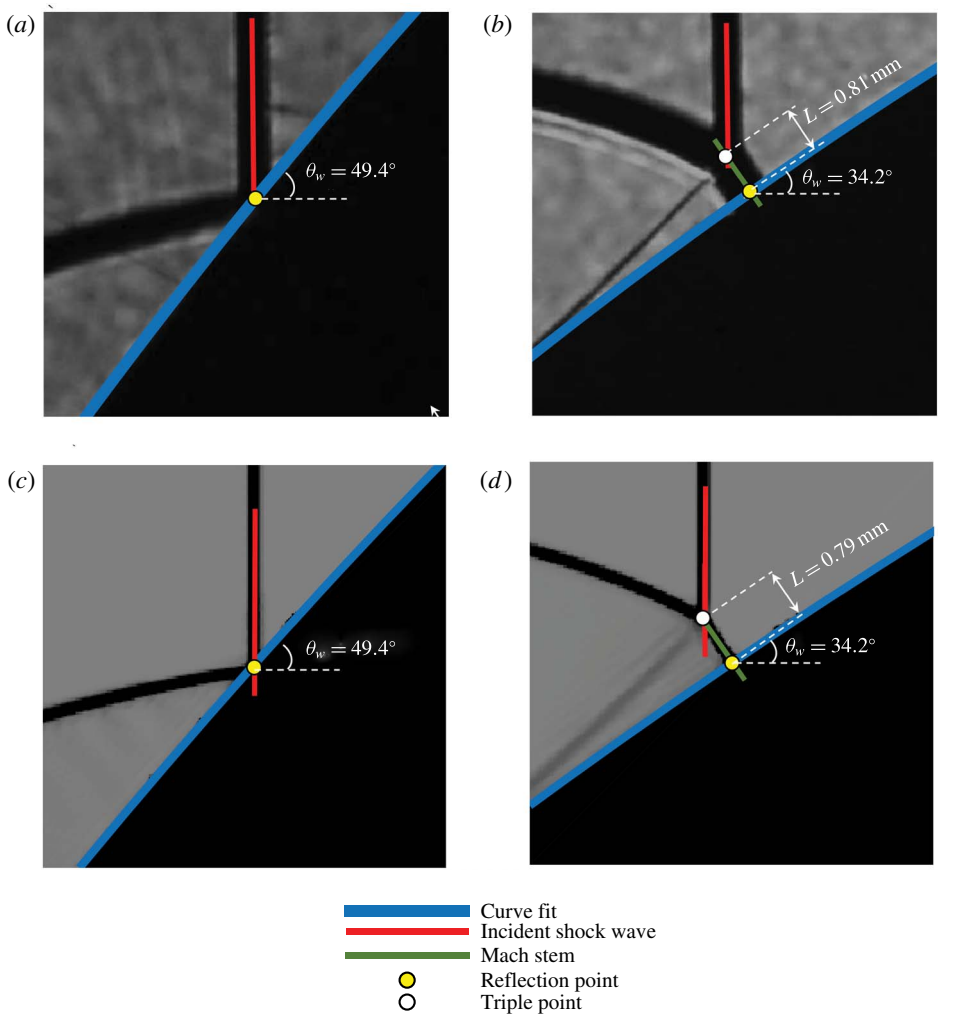


FIGURE 7. (Colour online) Image-processing analysis of the reflection area marked by red rectangles in figure 6: (*a*,*b*) experiments and (*c*,*d*) simulations.

and reflected shock waves when a wedge is inclined at an angle of 47.5°. This is consistent with the numerical results shown in figure 11(*a*). For the convex models, the radii dimensions clearly affect the reflected shock-wave orientations. As the radii dimension decreases, the orientation of the reflected shock wave deviates considerably from the horizontal line. The deviation is −3.9°, −6.3° and −7.5° for the 100, 70 and 40 mm models, respectively. The radii dimensions clearly affect the reflected shock-wave orientations, which in turn controls the thermodynamic properties behind the reflected shock wave. This is demonstrated in figure 11(*e–h*), where the flow Mach number distributions with respect to the reflection point are presented. The minimum flow Mach numbers, obtained adjacent to the reflection point, increase when the radii dimension decreases. Thus, any correlation between the two-shock theory and non-stationary flows during the reflection process is questionable (Ben-Dor & Takayama 1986; Hakkaki-Fard & Timofeev 2012; Kleine *et al.* 2014).

https://doi.org/10.1017/jfm.2017.835 Published online by Cambridge University Press

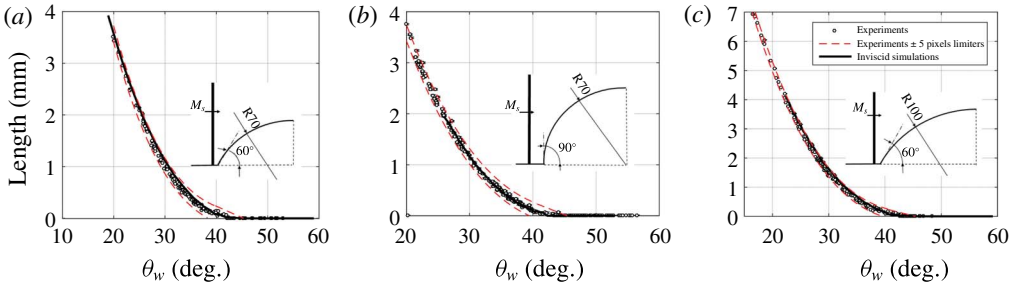


FIGURE 8. (Colour online) Experimental validation of the numerical computations performed at $M_s = 1.3$ for reflections over (*a*) model $R = 70$ mm, $\theta_i = 60°$; (*b*) model $R = 70$ mm, $\theta_i = 90°$; and (*c*) model $R = 100$ mm, $\theta_i = 60°$.

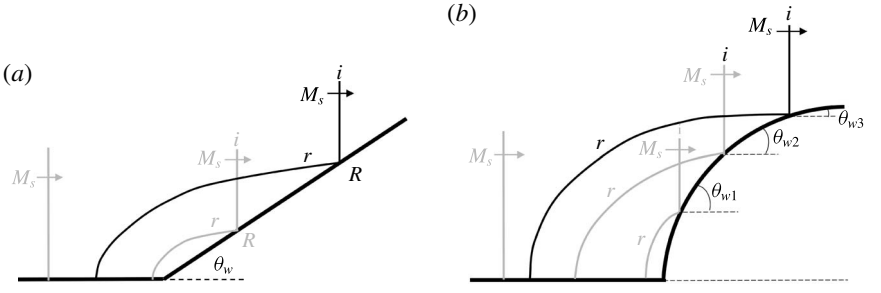


FIGURE 9. Schematic description of the RR configuration evolution in (*a*) pseudo-steady case and in (*b*) non-stationary case.

Since the RR evolution is dissimilar when considering pseudo-steady and non-stationary reflections, it is expected that the termination of an RR and the transition to an MR are not equivalent as well. Until now, locating the moment of transition was inherently difficult and imprecise. In many experimental studies, the RR→MR transition was determined to be the point where the Mach stem was first visualised. The Mach stem visualisation not only depends on the resolution of the experimental set-up but also locates the Mach stem long after its actual formation. High-resolution experiments may resolve the early stages of the Mach stem formation; however, the transition must be found by extrapolating the Mach stem length to zero. This extrapolation results in significant uncertainty originating from the low slope near the surface (Ram *et al.* 2015). So far, a suitable criterion to locate the transition does not exist. Hakkaki-Fard & Timofeev (2012) suggested that the criterion of the Mach-number-based technique is suitable for highly refined computations. According to this approach, when an RR exists, the entire flow along the surface in a frame of reference attached to the reflection point is supersonic. The MR evolves when a sonic point is reached, i.e. when at least one grid cell behind the reflected shock wave satisfies $M_2 = (U - u)/c \leqslant 1$, where U is the reflection point velocity along the surface and u and c are the flow velocity and speed of sound in the grid cell, respectively. Hakkaki-Fard & Timofeev (2012) and Kleine *et al.* (2014) stated that when applying the above formulation on a highly refined grid, the transition angle approaches the pseudo-steady criterion. In the present work, we were able to replicate this phenomenon. However, a subsonic flow behind the reflected shock wave is a

https://doi.org/10.1017/jfm.2017.835 Published online by Cambridge University Press

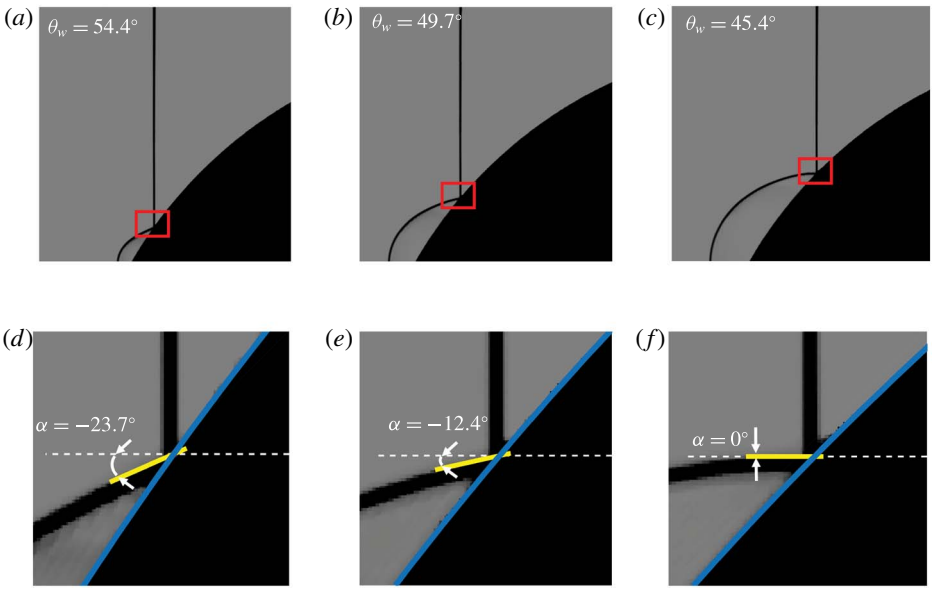


FIGURE 10. (Colour online) Evolution of the reflected wave inclination angles along the convex surface obtained by numerical simulations and computerised image processing. (*a–c*) Simulation results for a 40 mm convex model; (*d–f*) magnification of the images presented in (*a–c*) and the corresponding measured inclination angles of the reflected shock wave.

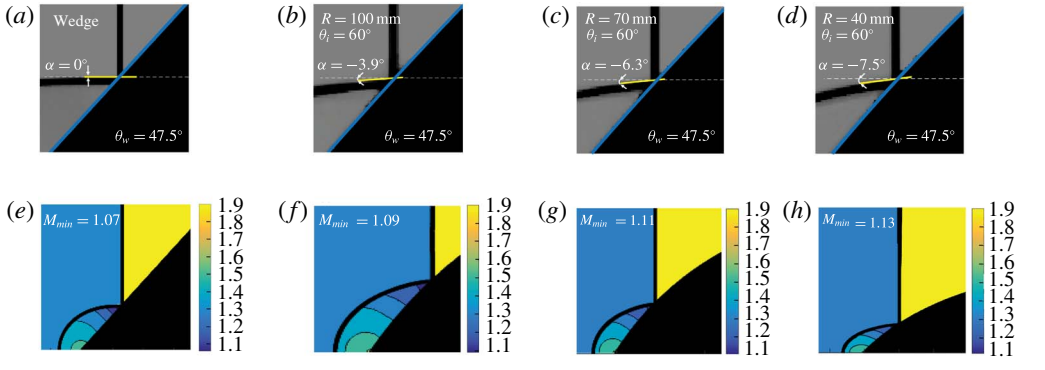


FIGURE 11. (Colour online) Reflection over convex models having the same initial angle at a surface angle of 47.5° and reflection over a wedge inclined at an angle of 47.5°. The magnifications of the computational results and the reflected shock-wave orientation are shown in (*a–d*). The Mach number distributions calculated by the Mach-number-based technique are shown in (*e–h*). (*a*,*e*) straight wedge; (*b*,*f*) $R = 100$ mm, $\theta_i = 60°$; (*c*,*g*) $R = 70$ mm, $\theta_i = 60°$; (*d*,*h*) $R = 40$ mm, $\theta_i = 60°$.

necessary condition for the existence of an MR but it is still an insufficient condition! Figure 12 demonstrates this claim.

For steady and pseudo-steady flows, the Mach-number-based technique is contradictory to the two-shock theory because it predicts an MR configuration in a domain in which only an RR exists. The transition angle corresponding to the detachment

https://doi.org/10.1017/jfm.2017.835 Published online by Cambridge University Press

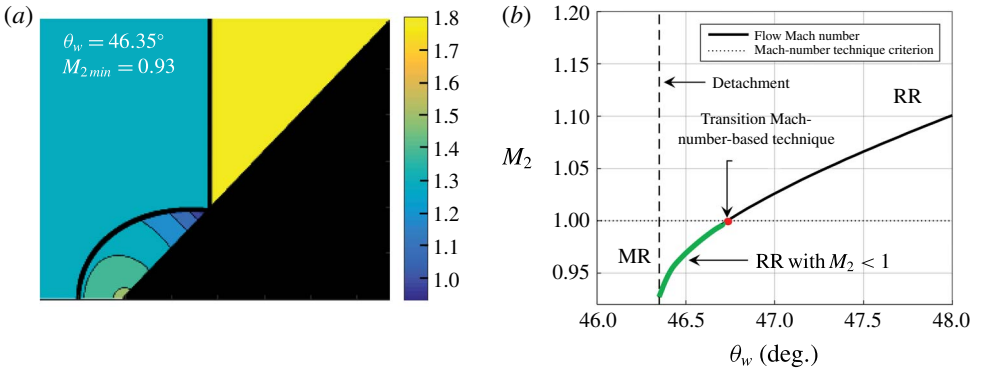


FIGURE 12. (Colour online) Flow Mach number in the frame of reference attached to the reflection point: (*a*) numerical Mach number distribution at $\theta_w = 46.35°$, and (*b*) analytical Mach number behind the reflected shock wave versus the surface angle for $M_s = 1.3$.

criterion at $M_s = 1.3$ is 46.345°. At a surface angle of 46.35°, an RR is still possible. According to the two-shock theory, the flow Mach number behind the reflected shock wave in the frame of reference attached to the reflection point is $M_2 = 0.928$. This is consistent with the numerical Mach number distribution computed by the above formulation (figure 12*a*). In fact, the Mach-number-based technique predicts the transition at a higher surface angle in a domain in which only an RR is possible (figure 12*b*). Because this criterion is not suitable for the steady and pseudo-steady flows, its use in non-stationary flows to determine the transition is arguable.

The elementary difference between the pseudo-steady and non-stationary reflections is the fact the reflected shock wave continuously adjusts to the varying surface angle. Consequently, its orientation changes in time, which alters the RR solution from self-similarity. In order to examine this transient mechanism it is necessary to measure the reflected shock angle evolution during the shock propagation along the surface. Figure 13 depicts the reflected shock wave angles with respect to the incident shock-wave motion direction plotted against the flow time. The automatic image processing procedure (Geva *et al.* 2013) was modified to evaluate these angles by fitting a linear line to a small straight part of the reflected shock wave near the wall and measuring its orientation. It should be noted that this measurement is inherently difficult. Properly fitting a linear line obliges selecting the largest possible section of the reflected shock wave near the wall. However, accounting for a distance, which is too long, degrades the quality of the fitting since the reflected shock wave becomes curved. Based on these limitations, figure 13(*a*,*b*) for Mach number 1.3 was plotted using a 1 mm length of the reflected shock wave. Whereas figure 13(*c*), accounting for Mach number 1.5, was plotted using 0.3 mm since higher Mach number increases the curvature of the reflected shock wave. In order to fit a shorter section of the reflected shock wave, a higher-resolution simulation was conducted for Mach number 1.5. The errors in these measurements were assessed by fitting lines that were 20 % longer and 20 % shorter.

As can be seen in figure 13, the reflected shock wave is compelled to change its orientation in time. During its propagation along the curved surface, the reflected shock wave does not only translates but also rotates about the reflection point. This phenomenon, which was overlooked in previous studies, is in complete contrast to pseudo-steady flows, in which the reflected shock wave has only a translation motion along the surface. This distinction is used for the modification of the 2ST which

https://doi.org/10.1017/jfm.2017.835 Published online by Cambridge University Press

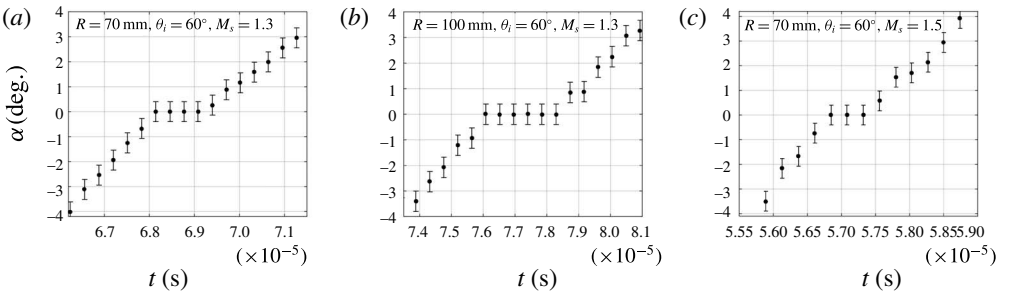


FIGURE 13. The variation in the reflected shock-wave angles, with respect to the horizontal line (α), along the flow time (*a*) $R = 70$ mm, $\theta_i = 60°$, $M_s = 1.3$; (*b*) $R = 100$ mm, $\theta_i = 60°$, $M_s = 1.3$; and (*c*) $R = 70$ mm, $\theta_i = 60°$, $M_s = 1.5$. The angle α is demonstrated in figure 10.

is presented in § 3.2.1. The modification is then successfully compared with the experimentally validated high-resolution numerical computations.

Another interesting observation, based on figure 13, is the inflection points that occur when the angle between the reflected shock wave and the incident shock-wave motion direction are zero. These inflections indicate that the reflected shock-wave rotation terminates when the waves are perpendicular. Just after the perpendicularity of the waves, the reflected shock wave continues to rotate. In § 3.2.2, a criterion for the non-stationary RR→MR transition will be given. As will be analytically explained by the 'no penetration' of the flow condition, the transition is at the moment in which the wave are perpendicular.

3.2.1. *Modification of the standard 2ST for convex surfaces*

In order to model correctly the reflections over curved surfaces, the curvature of the surface and the rotational velocity, $\dot{\alpha}$, must be attended. For the sake of the arguments that follow, the rotational velocity is evaluated as the time derivative of the angle α (i.e. slopes presented in figure 14). The rate at which the reflected shock wave changes its orientation depends on the radii dimensions. When radii are small, the reflected shock wave is forced to adjust itself faster to the changing conditions and therefore its rotation increases. Considering the above discussion, the fact that the reflected wave continually changes its orientation implies that additional physics, which is influenced by this non-inertial behaviour, must be considered.

The standard 2ST, which is suitable for pseudo-steady reflections, is solved when the reference frame is attached to the reflection point. Thus, the shock waves are considered stationary and the flow passes through the waves (figure 1*b*). Figure 15 illustrates the difference in the velocities entering the reflected shock waves when pseudo-steady and non-stationary RR are considered. In figure 15(*a*) the pseudo-steady RR configuration is presented. The flow enters the incident shock wave at M_0 and then it is deflected and is reduced to M_1. So the flow that enters the reflected shock wave is M_1 (figure 15*b*). When considering the RR over convex surface (figure 5*c*), in addition to M_1, the reflected shock wave advances towards the incident shock wave. As a result of this relative motion, an increase in the effective velocity that enters the reflected shock wave is obtained, M_1' (figure 15*d*). Each point along the reflected shock wave has a different velocity entering the wave at a different angle.

Another difference results from the curvature of the surface. Unlike the pseudo-steady case where the surface angle is constant (figure 16*a*). In convex surfaces,

https://doi.org/10.1017/jfm.2017.835 Published online by Cambridge University Press

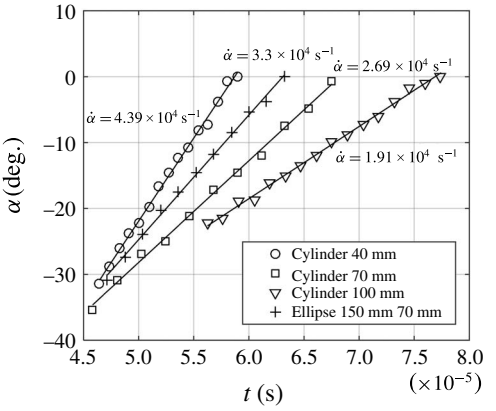


FIGURE 14. Inclination angle results for the cylindrical (*a*), (*b*), (*d*) models shown in figure 4 and elliptical model (*a*) shown in figure 5. The initial angle was not varied since it does not affect the transition (Kleine *et al.* 2014 and § 3.2.2). Inclination angle α is defined in figure 10.

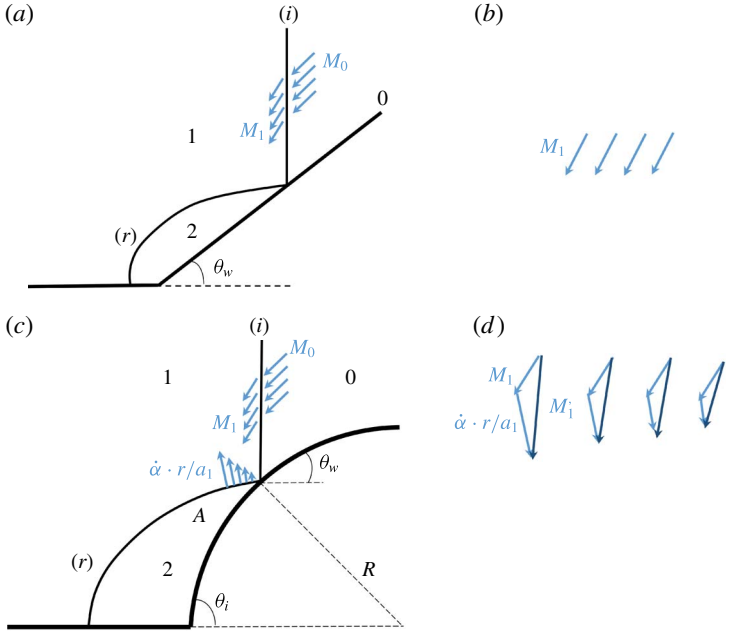


FIGURE 15. (Colour online) Schematic description of the velocity field in domains 0 and 1 when the waves are considered stationary: (*a*) pseudo-steady RR and (*b*) velocity entering the reflected shock wave in pseudo-steady reflection. (*c*) Non-stationary RR and (*d*) velocity entering the reflected shock wave in non-stationary reflection. a_1 is the speed of sound at domain 1 and r is the distance from the reflection point. $\dot{\alpha}$ is the rotational velocity obtained in figure 14.

the surface angle increases upstream from the reflection point. Since the incoming flow must be parallel to any local surface angle ('no-penetration' condition of the flow), the required deflection angle of the reflected shock wave is decreased along

https://doi.org/10.1017/jfm.2017.835 Published online by Cambridge University Press

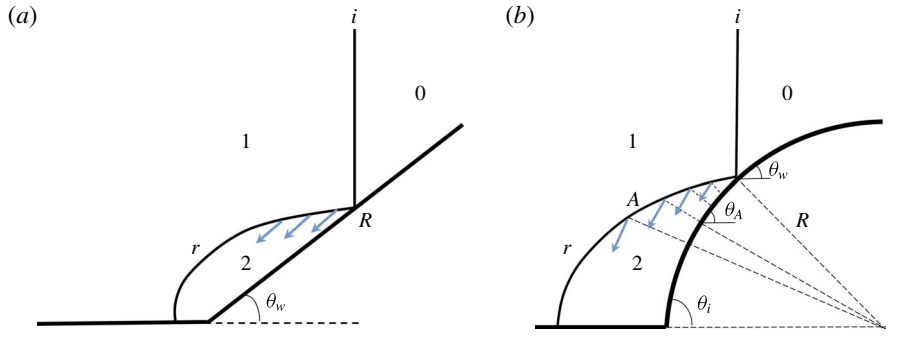


FIGURE 16. (Colour online) Schematic description of the flow field behind the reflected shock wave (*a*) pseudo-steady reflection and (*b*) non-stationary reflections.

the wave (figure 16*b*). Hence, the modified 2ST solution requires the modification of the velocity entering the reflected shock wave together with the modification of the required deflection angle. Since both depend of the distance from the reflection point, the reflected shock wave is divided into increments and the modification is calculated along each point.

Modified 2ST. As regards the calculation of the flow conditions across the incident shock wave, the modified 2ST that will be discussed here does not require any different analysis from that used in the standard 2ST. The conditions behind the incident shock are obtained by solving the standard oblique shock-wave relations (setting $j=1$ and $i=0$):

$$\theta_j = \tan^{-1}\left[\frac{(M_i^2\sin^2\phi_j - 1)\cot\phi_j}{\frac{\gamma+1}{2}M_i^2 - (M_i^2\sin\phi_j - 1)}\right], \tag{3.1}$$

$$M_j^2 = \frac{\left[1+\frac{1}{2}(\gamma-1)M_i^2\sin^2\phi_j\right]^2 + \left[\frac{1}{4}(\gamma+1)M_i^2\sin 2\phi_j\right]^2}{\left[1+\frac{1}{2}(\gamma-1)M_i^2\sin^2\phi_j\right]\left[\gamma M_i^2\sin^2\phi_j - \frac{1}{2}(\gamma-1)\right]}, \tag{3.2}$$

where $\phi_1 = 90^\circ - \theta_w$, $M_0 = M_s/\sin\phi_1$ and γ is the heat capacities ratio. Figure 17 shows the velocity behind the shock, M_1, and its orientation, $\phi_1 - \theta_1$. As for the reflected shock wave, consider an arbitrary point A along the reflected shock wave (figure 17). The effective velocity that enters the reflected shock wave is increased because of the relative motion of the waves. Consequently, the Mach number of the flow entering the reflected shock wave at an arbitrary point A is then calculated as follows:

$$M'_{1A} = \frac{|\bar{V}_1 + \bar{\bar{\alpha}}\times\bar{r}_A|}{a_1}, \tag{3.3}$$

where a_1 is the sound velocity behind the incident shock wave, and the fluid velocity $V_1 = M_1/a_1$ is calculated in the reference frame attached to the reflection point. The orientation of r_A with respect to the incident shock-wave motion is initially estimated by a random value of α. This value is then updated through an iterative procedure until a convergence of the energy equations was obtained. The required deflection angle through the reflected shock wave decreases and is modified as follows (figure 17):

$$\theta'_{2A} = \theta_1 - (\theta_w - \theta_A). \tag{3.4}$$

https://doi.org/10.1017/jfm.2017.835 Published online by Cambridge University Press

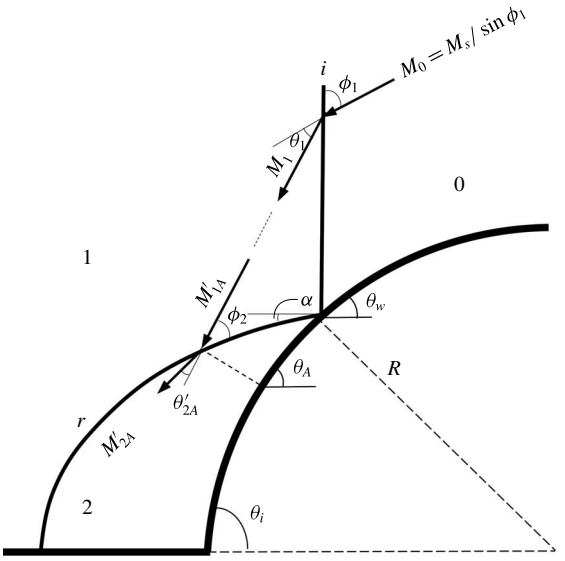


FIGURE 17. Deflection mechanism and flow domains over a convex surface: velocities, wave angles and turn angles related to the oblique shock-wave relations.

Note that the dependency of the reflecting surface on the curvature is embodied both in $\dot{\alpha}$ and in the surface angle at point A. Previous analytical approaches, which were presented in the introduction, failed to integrate this dependence. Substituting the modifications of the flow Mach number and the required deflection angle, equation (3.1) with $i = 1$ and $j = 2$ results in

$$\theta'_{2A} = \tan^{-1}\left[\frac{(M'^2_{1A}\sin\phi_2 - 1)\cot\phi_2}{\dfrac{\gamma+1}{2}M'^2_{1A} - (M'^2_{1A}\sin\phi_2 - 1)}\right]. \tag{3.5}$$

A better estimation for α can be found as $\alpha = 90° - (\phi_1 - \theta_1) - \phi_2$. The values of M'_{1A} and θ'_{2A} are updated with the improved estimation of α. Equation (3.5) can be solved again. One should note that if there is no change in the angle α, the solution converged and the conservation equations are satisfied. Following the modification, all the flow properties can now be evaluated with respect to point A. The entire flow field properties can be computed across the shock if the above-mentioned procedure is repeated over the entire reflected shock wave. For the reader's convenience, a numerical example is presented in § A.1.

Results of modification and discussion. Figure 18 depicts the analytical results (white lines) over the grey-scale results obtained by the numerical simulations. Figure 18(*a–c*) shows the full frame results for the cylindrical models. While figure 18(*d–f*) presents the magnification of the corresponding red squares in figure 18(*a–c*), respectively. Adjacent to the reflection point, a good agreement was obtained between the simulations and the analytical formulation. The reader should bear in mind that the rotational velocity used for the modification was estimated near the reflection point, where the reflected shock was reasonably straight. Maintaining this notion

https://doi.org/10.1017/jfm.2017.835 Published online by Cambridge University Press

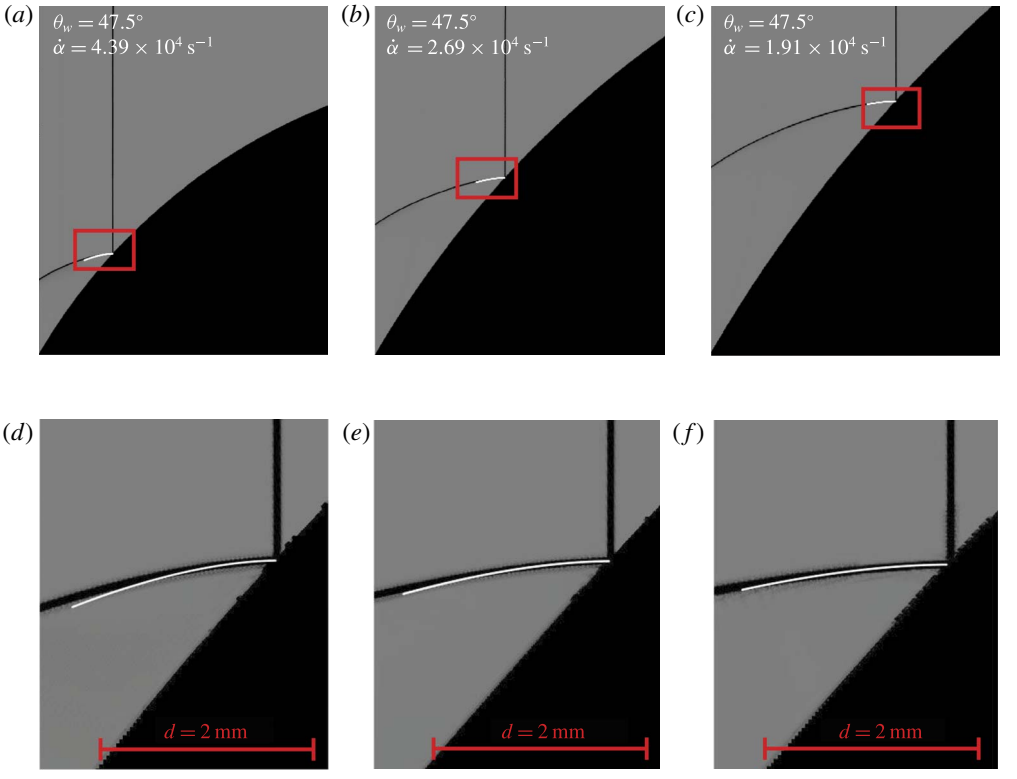


FIGURE 18. (Colour online) Modified 2ST calculated with $\dot{\alpha}$ obtained in figure 14 (marked by a white line). (*a–c*) Show the original images from the simulations. (*d–f*) Denote the magnifications: (*a*,*d*) $R = 40$ mm, $\theta_i = 60°$, (*b*,*e*) $R = 70$ mm, $\theta_i = 60°$; (*c*,*f*) $R = 100$ mm, $\theta_i = 60°$.

when the radii are small is more difficult because the wave rapidly grows and has a more pronounced curvature. However, the rotational velocity estimation seems to hold for a larger distance along the reflected shock wave as the radii of the model increases.

Figure 19 shows a solution at which an optimal rotational velocity was found to yield the best correlation to the numerical results along a 2 mm distance. The rotational velocity that was found was lower than the previously computed $\dot{\alpha}$ (figure 14). Figure 20 shows the optimal rotational velocities correlating to the numerical results at different distances along the reflected shock wave. The rotational velocity decreases when larger distances from the reflection point are considered. The same trend was obtained when the modified 2ST was applied for the elliptical model. The previously computed rotational velocity (figure 14) yielded a good correlation with the numerical results close to the reflection point (figure 21*a*,*d*). One should use a smaller rotational velocity for the modified solution to be applicable further away. The reflected shock waves presented in figure 21(*b*,*c*,*e*,*f*) were calculated with optimal velocities. These rotational velocities were plotted against the distance from the reflection point (figure 22). Similar to the cylindrical models, the rotational velocity of the reflected shock decreased with the increased distance from the reflection point. Therefore, applying the rotational velocity that was found based on a small

https://doi.org/10.1017/jfm.2017.835 Published online by Cambridge University Press

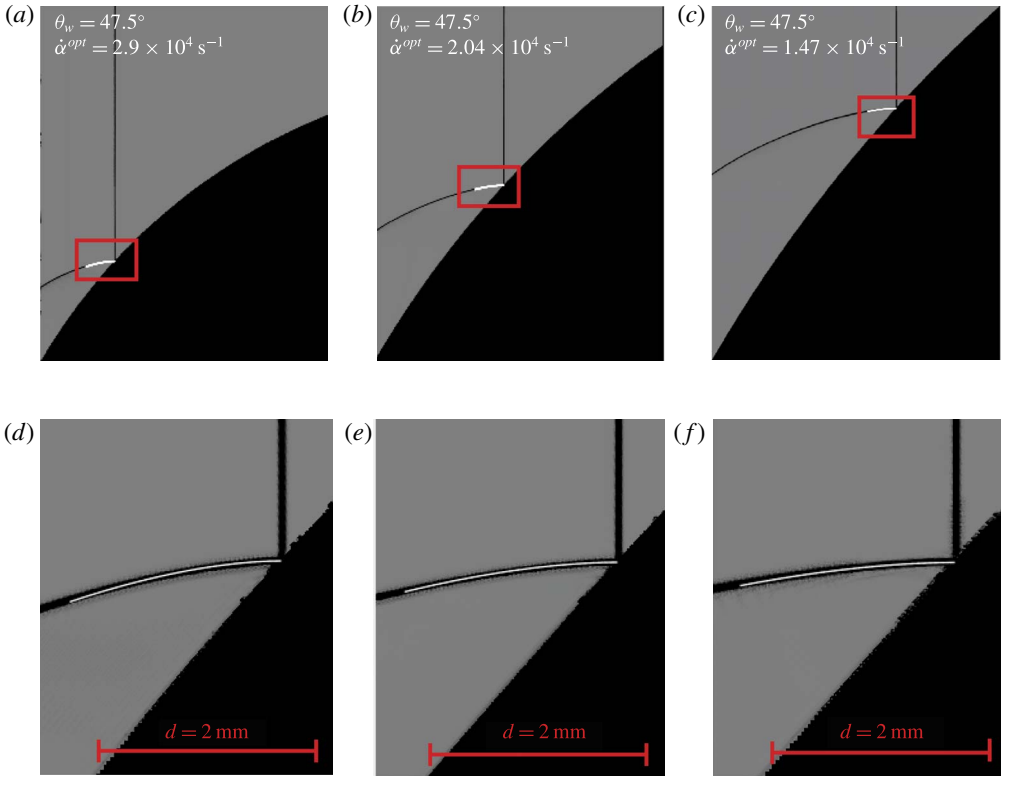


FIGURE 19. (Colour online) Results of the modified 2ST (marked with white lines) calculated with the optimal rotational velocity, $\dot{\alpha}^{opt}$. (*a–c*) Show the original images from the simulations. (*d–f*) Denote the magnifications. (*a*,*d*) $R = 40$ mm, $\theta_i = 60°$; (*b*,*e*) $R = 70$ mm, $\theta_i = 60°$; and (*c*,*f*) $R = 100$ mm, $\theta_i = 60°$.

straight part close to the reflection point was not suitable (figure 14). From a physical perspective, the modification corresponding to the rotational speed is necessary. Yet, the mathematical question on the proper evaluation of the rotational speed along the reflected shock remains open. The rotational velocity evaluation is usually performed using continuum mechanics methods. However, applying it here is impossible because it requires the association of points on the reflected shock at different times. The authors believe that the 'no-penetration' condition of the flow, which is presented in the following section of this study, can serve as an additional equation to determine the rotational velocity at each point along the reflected shock wave. As long as the rotational velocity is known, the modified 2ST can be applied to any point along the reflected shock wave. Since the modification is based on the fundamental condition of 'no penetration' of the flow, it is not restricted to the area near the reflection point. Yet the crucial area that relates to the transition is the region adjacent to the reflection point.

Figure 23(*a*) presents a comparison between the standard 2ST and the modified 2ST over a 70 mm cylinder. The radial velocity and the deflection angle corrections depend on the distance from the reflection point. Therefore, a very small correction is required. This deviation increases from the reflection point. Figure 23(*b*) graphically demonstrates the deviation by the shock polars. The *r*-polar of the modified 2ST starts

https://doi.org/10.1017/jfm.2017.835 Published online by Cambridge University Press

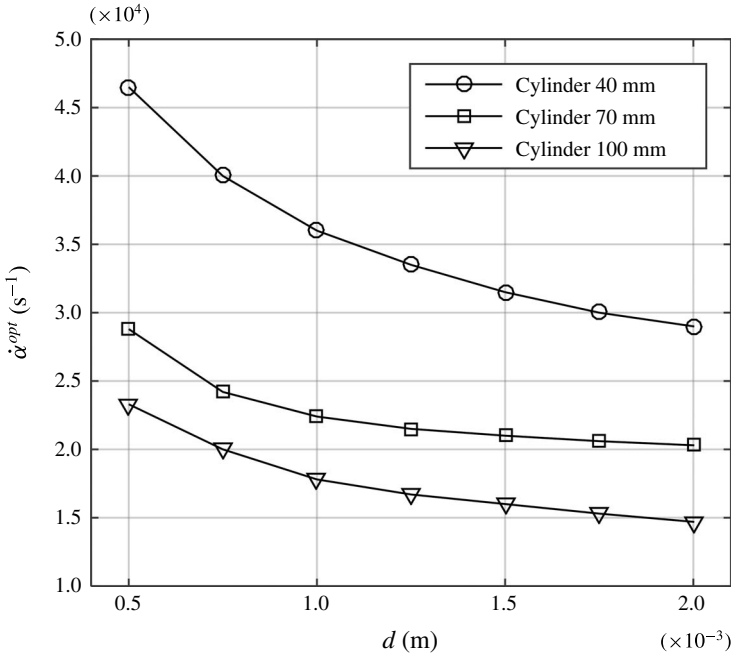


FIGURE 20. Optimum rotational velocity as a function of the distance from the reflection point, d, over cylindrical models.

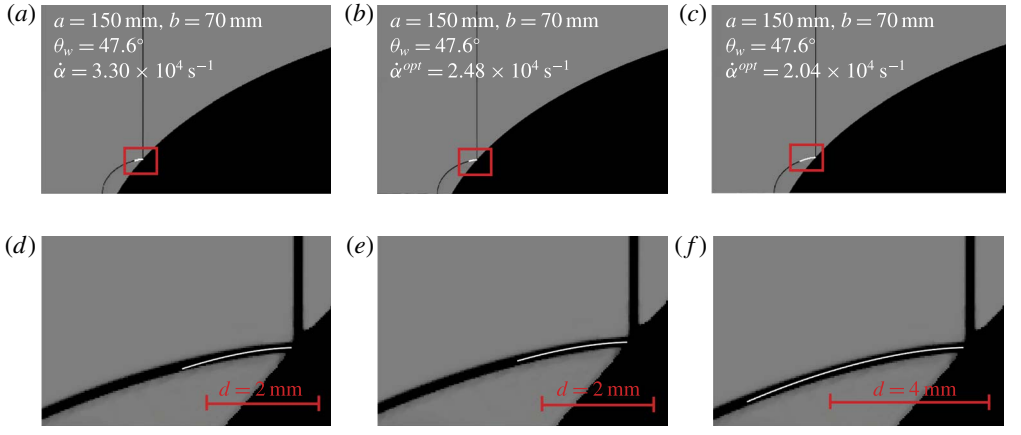


FIGURE 21. (Colour online) Results of the modified 2ST (marked by white lines) applied to the reflection over the ellipse. (*a–c*) Denote the original images from the simulations. (*d–f*) Present the magnifications. (*a*,*d*) Modified 2ST with computed in figure 14; (*b*,*e*) modified 2ST with the optimal rotational velocity for 2 mm length; and (*c*,*f*) modified 2ST with the optimal rotational velocity for the 4 mm length.

at θ_2', which is smaller than θ_2. In addition, the flow Mach number of the modified polar, M_1', is larger than that of the flow Mach number computed by the standard 2ST, M_1. The two-shock solution is obtained at the intersection of the r-polar with the vertical axis. One can see that the $p_2'/p_1 < p_2/p_1$.

https://doi.org/10.1017/jfm.2017.835 Published online by Cambridge University Press

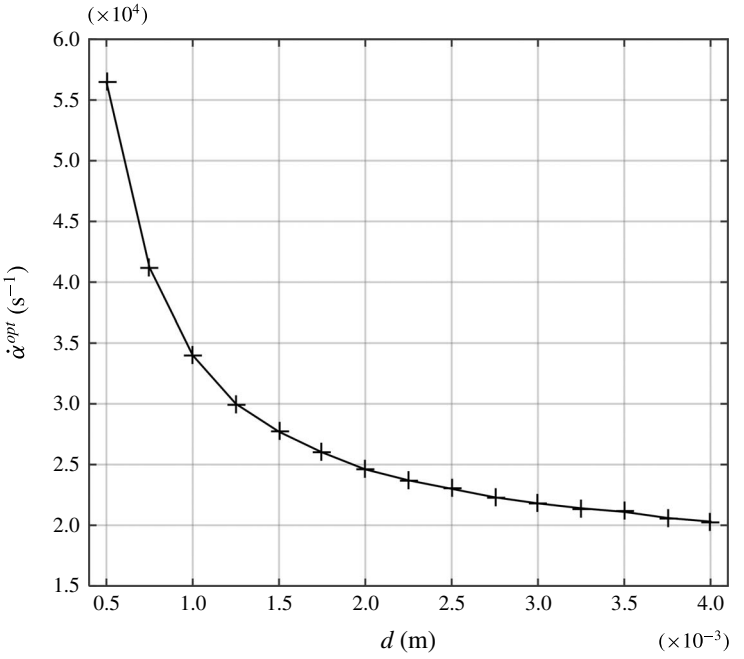


FIGURE 22. Optimum rotational velocity as a function of the distance from the reflection point, d, over the ellipse.

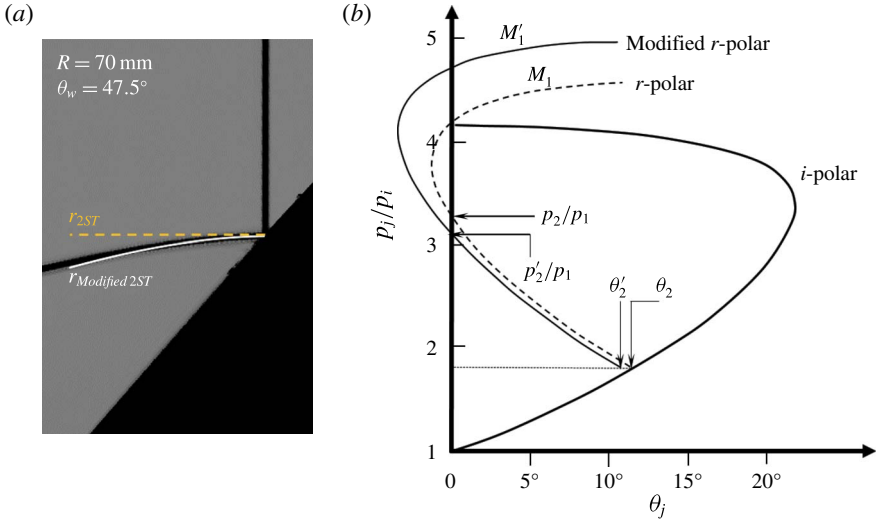


FIGURE 23. (Colour online) The difference between the standard and modified 2ST. (*a*) Resulting reflected shock wave obtained by the standard 2ST and by the modified 2ST over a 70 mm model. (*b*) Polar representation of the solutions.

These modified conditions make it easier for the flow to be deflected. Consequently, the RR can be retained for smaller surface angles in comparison with pseudo-steady flows. This explanation sheds new light on the transition criterion disagreements between the pseudo-steady and unsteady reflections. As the effective flow entering

https://doi.org/10.1017/jfm.2017.835 Published online by Cambridge University Press

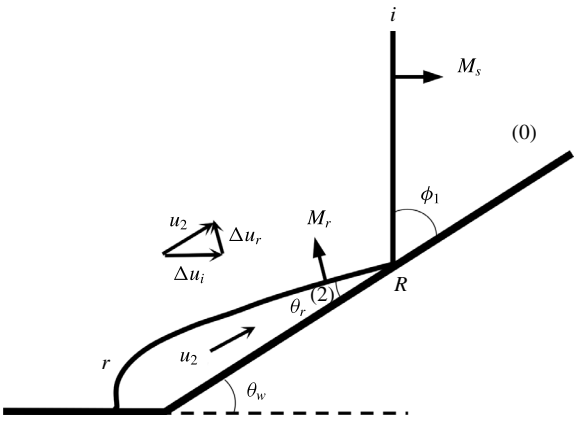


FIGURE 24. Schematic description of the flow regions in pseudo-steady RR.

the reflected shock wave is increased and the required deflection angle is decreased, the reflected shock-wave angle and the induced flow behind the reflected shock are decreased (for further explanation see § A.2). The rotation of the reflected shock wave alters the effective flow Mach number entering the reflected wave. This velocity is determined so the 'no-penetration' condition is maintained (as will be shown in the next section). For smaller radii, the rapid change in the surface angles affects both $\dot{\alpha}$ and the required deflection angle, θ_2'. Hence, a significant modification is needed and the delay in the transition will be more noticeable. This finding is consistent with the observation that the radius of curvature is the only available length scale over curved surfaces (Ram *et al.* 2015) and strengthens the claim that the transition angles depend of the radius of curvature (Takayama & Sasaki 1983; Ben-Dor 2007). No difference between the pseudo-steady and unsteady reflections was observed near the reflection point. Nevertheless, these data are insufficient in determining whether the transition criteria are similar (Hakkaki-Fard & Timofeev 2012; Kleine *et al.* 2014). Basing the transition criterion on the conditions very close to the reflection point is insufficient because the zone behind the reflection point that leads to the transition is unknown. Moreover, their observation that coarser grid numerical results depart from the pseudo-steady results can also be explained now. The shock waves in coarser grids tend to be thicker. Therefore, they force a large artificial modification in the required deflection angles, θ_2'. The MR is eventually formed when the RR can no longer sustain the required deflection of the flow. Consequently, in unsteady reflections, the increase in the flow Mach number along with the decrease in the required deflection angle will delay the transition.

3.2.2. *The physical mechanism that leads to transition at* 90° *inter-shock-waves angle*

The RR configuration is formed so that a supersonic flow can be negotiated about an obstacle. Consider the pseudo steady flow that is shown in figure 24. The induced flow behind the reflected shock wave, u_2, is parallel to the surface and the velocity component, which is perpendicular to the surface, is therefore zero ('no-penetration' condition).

The flow velocity along the surface behind the reflected shock wave in region 2 is given by:

$$u_2 = \Delta u_i \sin\phi_1 + \Delta u_r \sin\theta_r, \tag{3.6}$$

https://doi.org/10.1017/jfm.2017.835 Published online by Cambridge University Press

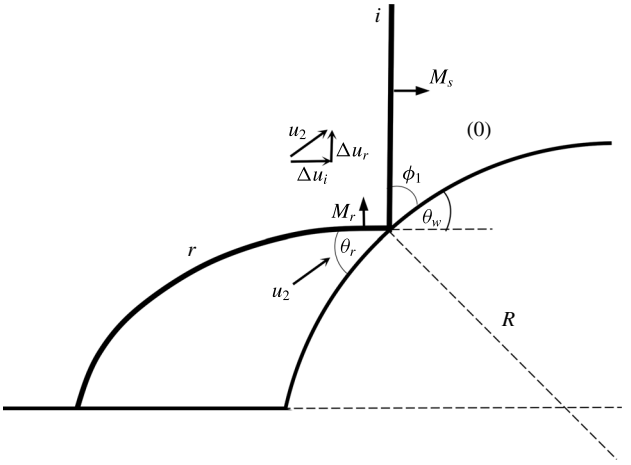


FIGURE 25. Unsteady RR configuration in which the reflected and incident shock waves are perpendicular.

where Δu_i and Δu_r are the induced flow velocities from the incident and the reflected shock waves, respectively. Due to the 'no-penetration' condition, the normal components of the induced flow velocities of the incident and reflected shock waves counter each other:

$$\Delta u_i \cos\phi_1 = \Delta u_r \cos\theta_r. \tag{3.7}$$

Hryniewicki, Gottlieb & Groth (2016) used (3.7) and constructed an error function

$$E(\theta_r) = 1 - \frac{\Delta u_r \cos\theta_r}{\Delta u_i \cos\phi_1}. \tag{3.8}$$

When this equals zero a solution for a regular reflection occurs. In other words, the reflected shock-wave angle is chosen in order to maintain the geometrical 'no-penetration' requirement.

The elementary requirement that the flow will not penetrate the surface exists in both pseudo-steady and unsteady flows. The particular moment at which the reflected shock becomes perpendicular to the incident shock wave was found to be the moment at which the RR→MR transition occurs. An explanation to this finding is that at this perpendicular angle equation (3.8) becomes identically zero. (This moment is illustrated in figure 25.):

$$1 - \frac{\Delta u_r}{\Delta u_i}\frac{\cos\theta_r}{\cos\phi_1} = 1 - \tan\theta_w \frac{\cos\theta_w}{\cos(90-\theta_w)} = 1 - \tan\theta_w \frac{\cos\theta_w}{\sin\theta_w} = 0. \tag{3.9}$$

Before the transition, in order for the 'no-penetration' condition to be held, a rotational velocity of the reflected shock wave must be introduced. This velocity causes an increase in the effective flow Mach number entering the reflected shock wave. As a result, the reflected shock-wave angle and the induced flow behind the reflected wave are reduced so (3.8) is maintained. The analytical justification is consistent with the findings presented in figure 11. As the radius decreases, higher rotational velocities are involved enabling the configuration to adjust quickly to the changing surface. This

https://doi.org/10.1017/jfm.2017.835 Published online by Cambridge University Press

in turn is possible only if the angle between the reflected and incident shock waves increases.

The particular 90° inter angle between the incident and reflected shock waves enables the existence of an RR without the need of an additional rotational velocity. Indeed, it was demonstrated in figure 13 that when the reflected shock wave is perpendicular to the incident shock wave, the rotation of the reflected shock wave reaches zero. Soon after, the reflected shock wave is no longer perpendicular to the incident shock wave. The only way to enable an RR, so that (3.8) is held, is by introducing an additional rotational velocity of the reflected shock wave. Due to the inertial movement of the flow around the shock wave, the buildup of the rotational velocity cannot transpire immediately. The delay in the rotational velocity buildup is demonstrated in the inflections of the rotational velocity shown in figure 13. Since an RR cannot deflect the flow so that 'no-penetration' condition is held, MR is then formed. The geometrical fundamental obligation of 'no penetration' is the criterion for the RR→MR transition in unsteady reflection.

The use of a highly refined computational mesh and high-resolution experiments enabled us to observe that this intriguing behaviour happened near the RR→MR transition. It was evident from both methods that an MR could not be formed if the angle between the incident and reflected shock waves was larger than 90°. It was very difficult to decide if this 90° angle was the precise angle at transition considering the above listed methods to determined transition. However, based on the high-resolution findings, it was reasonable to assume that the transition occurred very close to this point at moderate incident shock-wave Mach numbers.

Figure 26 depicts the perpendicular behaviour of the reflected and incident shock waves for reflections over models (*a–d*) near the transition point. Corresponding to the inflections in figure 13, the perpendicularity was observed to sustain over a certain period. The ranges of the corresponding surface angles at which this behaviour was evident are given in table 1. Optical limitations and changing the simulation time increments may slightly vary these ranges. Geometrical dependence of the perpendicularity is obtained in term of a slight increase in the transition angle when the radius of the model increases. For cylindrical model (*d*), which has a 100 mm radius, the transition was found to be similar to the pseudo-steady criterion. The effect of the initial angle on the transition angle was also examined by using two models having 70 mm radii and initial angles of 60 and 90°. Similar to the findings in Skews & Kleine (2010), it was found that the initial angle did not influence the transition. Figures 26(*f*) and 26(*h*) show the magnification of the red regions shown in figures 26(*b*) and 26(*d*), respectively. The horizontal behaviour of the reflected shock waves adjacent to the reflection is apparent at the same surface angle (table 1). This also reinforces the notion that the perpendicularity of the waves and the corresponding transition depends on the geometric scaling.

For the case of reflections over the elliptical models, a geometric scaling was also observed. In these cases, due to the varying curvature, a varying rate of change is imposed on the transition process. Table 2 presents the surface angles of the ellipses corresponding to the moment in which the perpendicularity behaviour of the shock waves was observed. Figure 27 demonstrates the perpendicularity of the reflected and incident shock waves over the elliptical models. For the ellipse with a decreasing radius of curvature (model *b*), the transition angle is closer to the detachment criterion and is similar to the transition angle found for reflections over the 100 mm cylindrical model. For the elliptical model with an increasing radius of curvature (model *a*), the transition angle is similar to the transition angle obtained for reflections over the

https://doi.org/10.1017/jfm.2017.835 Published online by Cambridge University Press

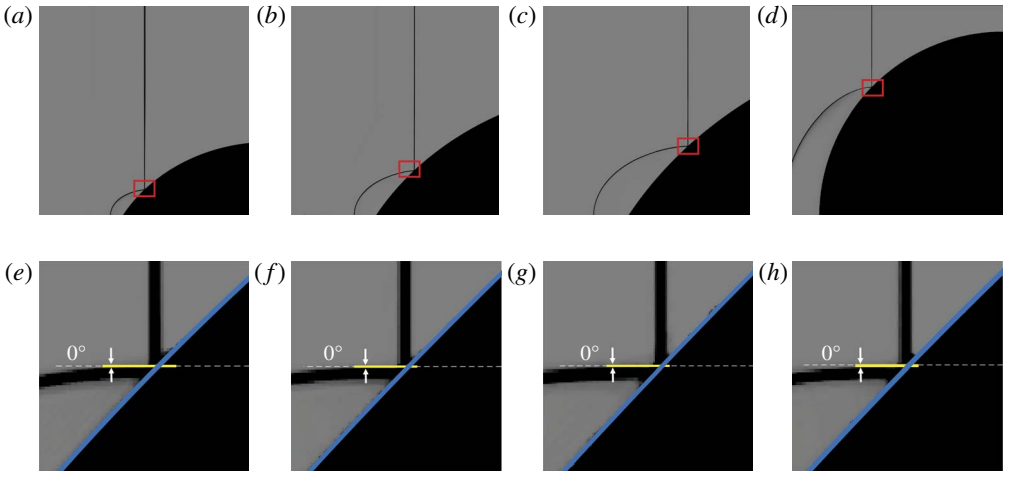


FIGURE 26. (Colour online) Simulation results for reflections over models (*a–d*) near the transition angles (table 1). The original images from the computations are shown in (*a–d*). The magnification of the areas marked by red squares of the results and the reflected shock-wave orientation as extracted by the program are shown in (*e–h*). (*a*,*e*) $R = 40$ mm, $\theta_i = 60°$, $\theta_w = 45.4°$; (*b*,*f*) $R = 70$ mm, $\theta_i = 60°$, $\theta_w = 45.8°$; (*c*,*g*) $R = 100$ mm, $\theta_i = 60°$, $\theta_w = 46.3°$; (*d*,*h*) $R = 70$ mm, $\theta_i = 90°$, $\theta_w = 45.8°$.

Model	Radius (mm)	Initial angle (deg.)	θ_w when waves are perpendicular (deg.)
a	40	60	45.4 ± 0.5
b	70	60	45.7 ± 0.4
c	70	90	45.7 ± 0.3
d	100	60	46.3 ± 0.4[a]
Detachment criterion			46.345

TABLE 1. Surface angles corresponding to the horizontal behaviour of the reflected shock wave over cylindrical surfaces.

[a]The upper boundary of the theoretical error is limited by the detachment criterion.

70 mm cylindrical model. This deviation implies that geometrical scaling may be a solution to eliminate this discrepancy. Using Pratt (1987) method, a circle was fitted to the area after the transition to describe the MR growth (figure 28), and the scale that was found appropriate for the transition was the best-fit circle prior to the transition ($46° \leqslant \theta_w \leqslant 60°$). The radii of the resulting equivalent circles are 68 and 93 mm for models (*a*) and (*b*), respectively (figure 28). In fact, as long as a circle can be fitted, the surface curvature does not play a role in the determination of the transition.

Figure 29 demonstrates the perpendicularity of the reflected shock wave near the transition points that was obtained experimentally. The Mach stems were measured in the following frames, and the angles between the incident and reflected shock waves were found to be smaller than 90°. Figure 29(*g*) demonstrates the inflection process as was obtained experimentally. The surface angles at which the reflected shock wave was horizontal, i.e. perpendicular to the incident shock wave, were found

https://doi.org/10.1017/jfm.2017.835 Published online by Cambridge University Press

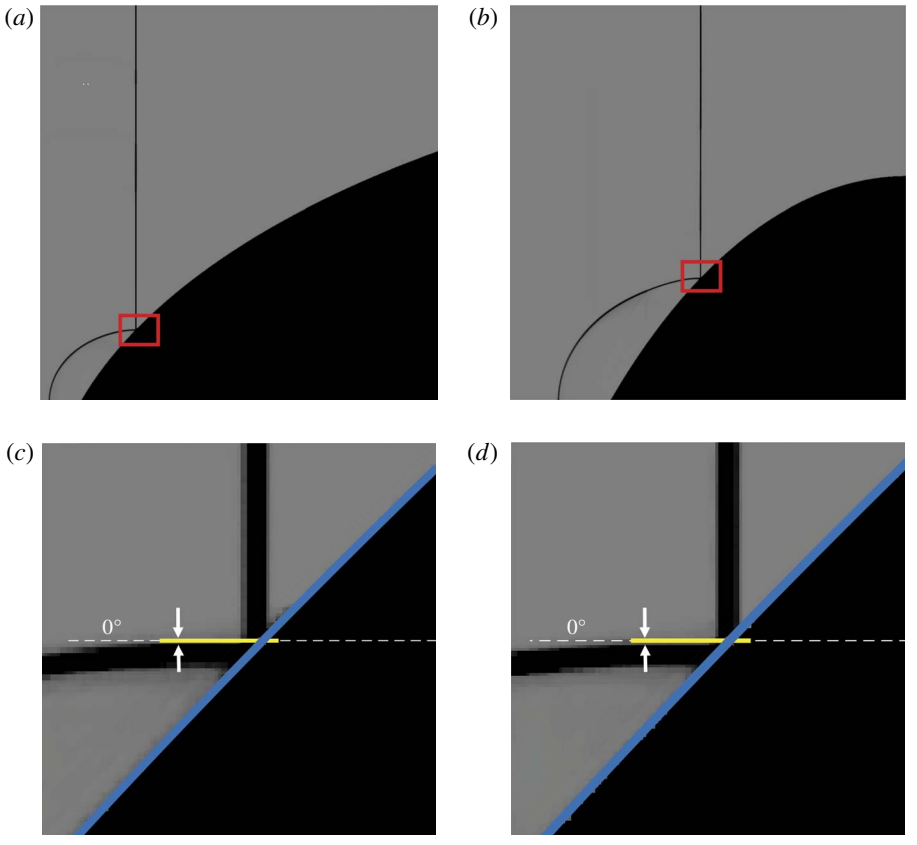


FIGURE 27. (Colour online) Simulation results for reflections over elliptical models near the transition (table 2). (*a*,*b*) The original images obtained by the computations. (*c*,*d*) The magnification of the areas marked by red squares and the reflected shock-wave orientation extracted by the program. (*a*,*c*) $a = 150$ mm, $b = 70$ mm, $\theta_i = 60°$, $\theta_w = 45.8°$; (*b*,*d*) $a = 70$ mm, $b = 150$ mm, $\theta_i = 90°$, $\theta_w = 46.2°$.

Model	Radii (mm)	Initial angle (deg.)	θ_w when waves are perpendicular (deg.)
a	$a = 150$ $b = 70$	60	$45.8 + 0.5$
b	$a = 70$ $b = 150$	60	46.2 ± 0.3
Detachment criterion			46.345

TABLE 2. Surface angles corresponding to the horizontal behaviour of the reflected shock wave over elliptical surfaces.

to be consistent with the transition angles obtained by extrapolation, with the former method having the advantage of producing smaller uncertainties.

The perpendicularity that was found to exist in both experiments and simulations could be regarded as a geometrical criterion for the RR→MR transition. Incidentally, this 90° condition is similar to the condition suggested by Shirouzu & Glass (1986) for the transition between a single Mach reflection and transitional Mach reflection

https://doi.org/10.1017/jfm.2017.835 Published online by Cambridge University Press

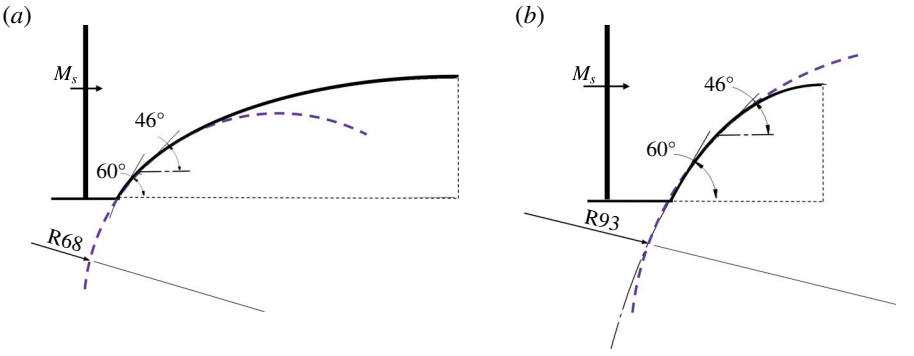


FIGURE 28. Best-fit circle to the ellipse in the area prior to the transition at surfaces angles $46° \leqslant \theta_w \leqslant 60°$: (*a*) a circle with a 68 mm radius is fitted to an ellipse with an increasing radius of curvature, and (*b*) a circle with a 93 mm radius is fitted to an ellipse with a decreasing radius of curvature.

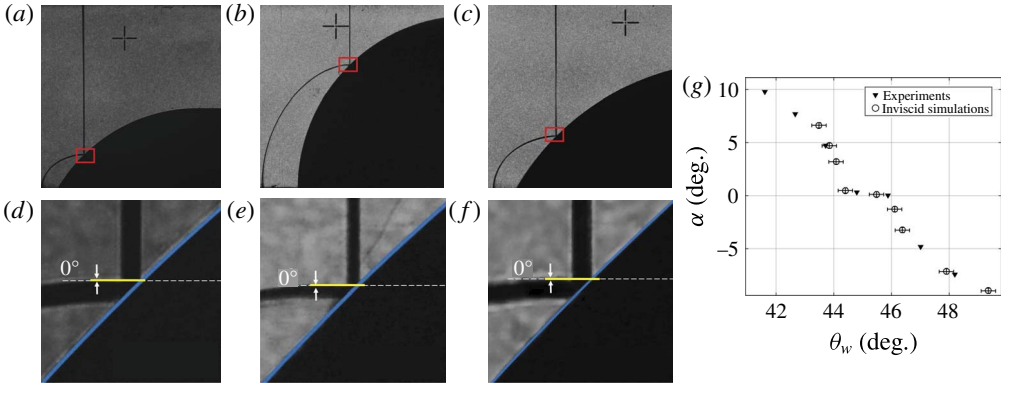


FIGURE 29. (Colour online) Experimental results for reflections over cylindrical models at angles at which the reflected shock is horizontal. (*a–c*) The original images from the experiments. (*d–f*) The magnification of the areas marked by red squares of the results and the reflected shock-wave orientation. (*a*,*d*) $R = 70$ mm, $\theta_i = 60°$, $\theta_w \approx 45°$; (*b*,*e*) $R = 70$ mm, $\theta_i = 90°$, $\theta_w \approx 45°$; (*c*,*f*) $R = 100$ mm, $\theta_i = 60°$, $\theta_w \approx 46°$; (*g*) variation of the reflected shock-wave angle along the surface for $R = 70$ mm, $\theta_i = 60°$.

in pseudo-steady reflections. Until now, the rotation of the reflected shock wave was not considered significant and its existence was neglected. However, it was demonstrated that the rotation of the reflected shock wave affects the RR evolution and its termination. The RR evolution and transition to MR waves are perpendicular, stem from the 'no penetration' of the flow condition. Which is a fundamental condition that must be held for any flow that passes over any solid body. While performing experiments, it is considerably easier to visualise the perpendicularity of the reflected and incident shock waves. Rather than the incorrect determination based on the appearance of a Mach stem or to carry out the more complicated and uncertain task of measuring the Mach stem length and extrapolating it to zero (Kleine *et al.* 2014; Ram *et al.* 2015).

https://doi.org/10.1017/jfm.2017.835 Published online by Cambridge University Press

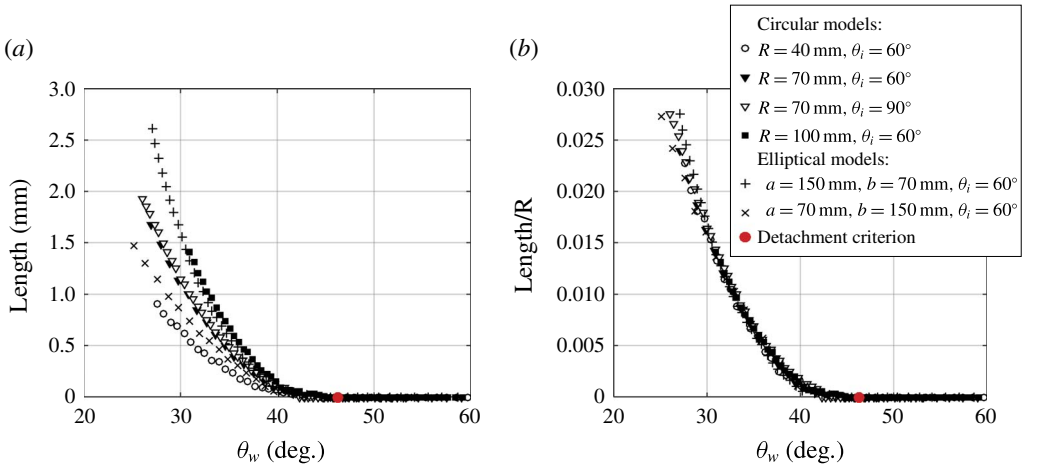


FIGURE 30. (Colour online) Simulation results of the Mach stem length for reflections over cylindrical and elliptical models: (*a*) Mach stem length versus the corresponding surface angle and (*b*) normalised Mach stem length versus the corresponding surface angle.

3.3. *Geometry governing Mach stem growth over convex surfaces*

Following the formation of the MR, the obtained wave configuration is a direct Mach reflection and the Mach stem grows as the surface angle decreases (Ben-Dor 2007). The triple point trajectories obtained from the simulations are plotted in figure 30(*a*). For cylindrical models, having a large radius of curvature, the growth of the Mach stems is faster than that for smaller radii. This is expected because as the radius increases, the amount of flow that must be deflected also increases. The similarity between our case and that of Kleine *et al.* (2014) enabled us to normalise the Mach stem length with the cylinder radius. The resulting normalised triple point trajectories are plotted in figure 30(*b*). The most noteworthy observation is that a change in the initial angle, i.e. 60° and 90°, does not affect the Mach stem growth, as can be seen in figure 30(*a*), where both the curves for the 70 mm radius coincide (triangular markers). The joined normalised curve demonstrates the consistent behaviour of the Mach stem growth over cylindrical convex surfaces having different radii of curvature and initial angles.

Regarding the elliptical models, both the trajectories for reflections over the elliptical surfaces fall within the trajectories of the cylindrical models. It is interesting to note that the normalisation parameter was not related to the geometrical shape of the ellipse. Different parameters that were ellipse oriented were examined, e.g. radius of curvature, distance from foci and in-circles. However, none of them was suitable. Surprisingly, the appropriate normalisation scale was the radius of the best-fit circle at surface angles in the range $30° \leqslant \theta_w \leqslant 45°$. The circles were obtained using the Pratt method (Pratt 1987), and the computed circles are plotted in figure 31. The suitable normalisation radii were 95 and 54 mm for ellipses (*a*) and (*b*), respectively (figure 31). The normalised trajectories of the elliptical models coincide with those of the cylindrical models. This significant finding leads to the conclusion that regardless of the geometrical shape and its characteristic size, if a circle can be fitted, the growth of the Mach stem can be found.

The aforementioned finding also reinforces the difference between pseudo-steady and non-stationary reflections in which a circle can never be fitted to a straight wedge.

https://doi.org/10.1017/jfm.2017.835 Published online by Cambridge University Press

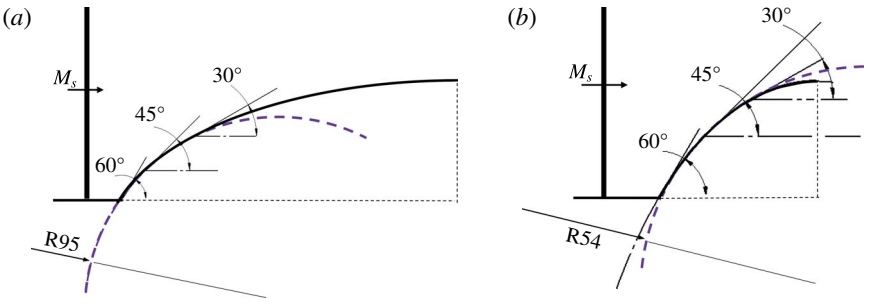


FIGURE 31. (Colour online) Best-fit circle to the ellipse in the area just after transition at surface angles in the range $45° \leqslant \theta_w \leqslant 30°$: (*a*) a circle with a 95 mm radius fitted to an ellipse with an increasing radius of curvature, and (*b*) a circle with a 54 mm radius fitted to an ellipse with a decreasing radius of curvature.

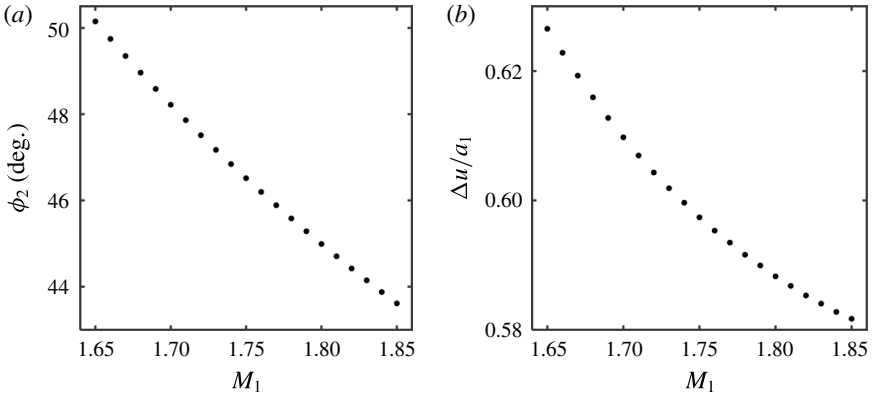


FIGURE 32. The reflected shock-wave angle and the induced flow Mach number behind the wave as a function of the flow Mach number at $\theta_1 = 10.7°$. (*a*) Was computed using (A 6) and (*b*) was computed using (A 7).

Conversely, the simplification of a circle-like assumption is not suitable for larger Mach stems. As the Mach stem grows, it is influenced not only by the surface curve but also by far-field effects. Therefore, additional parameters must be accounted for when evaluating the Mach stem length at smaller surface angles when the Mach stem is no longer perpendicular.

To find the geometrical parameters that influence the Mach stem buildup, several parameters were analysed. It was found that neither the initial angle nor the varying rate of curvature change is related to the buildup. Instead, the only geometrical dependency is in the radius of the surface. Even when considering a non-circular shape, the problem can be normalised by finding the best-fit circle. This geometrical dependence in the Mach stem growth is consistent with the geometrical dependence found to be dominant when RR was evident. This simple geometrical dependence reduces the complexity of the analysis of the reflection over convex surfaces and the complexity in the RR→MR transition in particular.

https://doi.org/10.1017/jfm.2017.835 Published online by Cambridge University Press

4. Conclusions

In this study, the non-stationary reflections over cylindrical and elliptical convex models were analysed numerically. Numerical computations were validated by experiments with extremely high spatial resolutions, thus enabling features as small as 0.06 mm to be resolved. The influence of the radius of the surface, initial angle, and varying rates of surface change were examined in the context of the RR evolution, RR→MR transition and Mach stem growth. It was found that the only geometrical parameter that affected the reflected is the radios of the surface. Regardless of the geometry involved, as long as a circle could be fitted to the surface, the radius of the best-fit circle was the characteristic length of the problem. This simplification eliminated all kinds of geometrical shape–oriented parameters and reduced the problem complexity considerably.

Unlike the self-similarity in pseudo-steady reflections, in non-stationary flows the reflection configuration is not self-similar. The curved surface imposes the reflected shock wave a changing boundary conditions. The reflected shock orientation is varied as it responds to the continuous change in the surface angle. For the first time, the existence of the reflected shock-wave rotation about the reflection point was examined. This behaviour was demonstrated at Mach numbers 1.3 and 1.5. Based on the 'no-penetration' condition of the flow the evolution of and RR and its transition to MR were explained. When smaller radii are introduced, the reflected shock wave adjusts itself quicker to the changing surface, resulting in a higher rotation. In order for the no penetration of the flow to be held, the angle between the incident and reflected shock waves increases and the configuration deviates considerably from the pseudo-steady case. It was found that when the waves are perpendicular the rotation vanishes and the 'no-penetration' condition is identically zero. The high-resolution experimental and computational results revealed that this moment is the moment of RR→MR transition. The perpendicularity of the incident and reflected shock waves was easier to resolve when performing experiments. Therefore, we propose using this criterion as the RR→MR transition criterion rather than using the methods known today. In this study, this feature together with the curvature of the surface were introduced to the oblique shock wave relations. Consequently, the two-shock theory was successively modified to account for the fact that the reflection is non-stationary.

Acknowledgements

This research was supported by the Israel Science Foundation (grant no. 1045/15). We thank Professor G. Ben-Dor for his useful discussions on our paper. O.R. is supported by the Adams Fellowship program of the Israeli Academy of Science and Humanities.

Appendix A

A.1. *The modification of the 2ST*

We consider the following input: $M_s = 1.3$; $R = 40$ mm; $\theta_w = 47.62°$, and $\dot{\alpha} = 4.397 \times 10^4$ s^{-1}. The wave angle (i.e. $\phi_1 = 42.38°$) and the flow Mach number (i.e. $M_0 = 1.3/\sin(42.38°)$) for the incident shock wave was substituted in (3.1) and (3.2) (setting $j = 1$, $i = 0$). We obtain the following values:

$$\left.\begin{aligned} M_1 = 1.524, \quad \theta_1 = 11.33°, \quad T_1 = 357.25 \text{ K}, \\ V_1 = M_1 a_1 = 577.4 \text{ m s}^{-1}, \\ V_{1x} = V_1 \sin(\phi_1 - \theta_1) = 297.77 \text{ m s}^{-1}, \\ V_{1y} = V_1 \cos(\phi_1 - \theta_1) = 494.69 \text{ m s}^{-1}. \end{aligned}\right\} \tag{A 1}$$

https://doi.org/10.1017/jfm.2017.835 Published online by Cambridge University Press

	Simulation	Analytical	Relative error (%)
V_2' (m s^{-1})	515.33	515.01	0.06
T_2 (K)	413.17	413.94	0.18

TABLE 3. Comparison between the numerical and analytical values at the point located in $r_A = 1.09 \times 10^{-3}$ m.

The procedure that follows must be computed at each point along the reflected shock wave to solve the entire reflected shock wave. For an arbitrary point A located at $r_A = 1.092 \times 10^{-3}$ m away from the reflection point, we start by guessing the orientation of r_A, α.

First iteration

Guessing $\alpha = 9°$ and evaluating the modified values of the flow Mach number ahead of the shock and the deflection angle with (3.3)–(3.4) lead to:

$$\left.\begin{aligned} M_{1A}' &= \frac{|\bar{V}_1 + \omega \cdot \bar{r}_A|}{a_1} = \frac{|V_{1x}\hat{i} + V_{1y}\hat{j} + \dot{\alpha} r_A \cdot (-\sin\alpha\hat{i} + \cos\alpha\hat{j})|}{a_1} = 1.6237, \\ \theta_2' &= \theta_1 - (\theta_A - \theta_w) = 10.128°, \quad \text{where } \theta_A = f(R, r_A, \alpha) = 48.821°. \end{aligned}\right\} \tag{A 2}$$

We find the shock-wave angle ϕ_2 for the reflected shock wave ($j = 2$ and $i = 1$) from (3.5) as follows:

$$\phi_2 = 50.284° \quad \rightarrow \quad \alpha = 90° - (\phi_1 - \theta_1) - \phi_2 = 8.66°. \tag{A 3}$$

One should repeat the iteration until convergence if α is not equal to the guessed value ($\alpha = 9°$ in the present case).

Second iteration

Continuing the process with $\alpha = 8.66°$ and evaluating the modified values of the flow Mach number ahead of the shock and the deflection angle with (3.3)–(3.4) lead to:

$$\left.\begin{aligned} M_{1A}' &= \frac{|\bar{V}_1 + \omega \cdot \bar{r}_A|}{a_1} = \frac{|V_{1x}\hat{i} + V_{1y}\hat{j} + \dot{\alpha} r_A \cdot (-\sin\alpha\hat{i} + \cos\alpha\hat{j})|}{a_1} = 1.6241, \\ \theta_2' &= \theta_1 - (\theta_w - \theta_A) = 10.134°, \quad \text{where } \theta_A = f(R, r_A, \alpha) = 48.816°. \end{aligned}\right\} \tag{A 4}$$

We find the shock-wave angle ϕ_2 for the reflected shock wave ($j = 2$ and $i = 1$) from (3.5) as follows:

$$\phi_2 = 50.277° \quad \rightarrow \quad \alpha = 90° - (\phi_1 - \theta_1) - \phi_2 = 8.67°. \tag{A 5}$$

The calculated angle α is practically the same as the initial guess ($\alpha = 8.66°$). Therefore, the conservation equations are satisfied across point A. Table 3 demonstrates the good agreement obtained between the numerical and analytical results.

https://doi.org/10.1017/jfm.2017.835 Published online by Cambridge University Press

A.2. *The shock-jump relation of an oblique shock wave*

This section explains how an increase in the effective Mach number entering the reflected shock wave causes a decrease in both the reflected shock-wave angle and the induced flow Mach number behind the reflected shock wave.

The relation between the deflection angle (θ), the shock angle (ϕ) and the flow Mach number entering the shock wave (M_i) is given by

$$\tan\theta_j = \frac{(M_i^2 \sin^2\phi_j - 1)\cot\phi_j}{1 + M_i^2\left(\frac{\gamma+1}{2} - \sin^2\phi_j\right)}. \tag{A 6}$$

From the above equation, for a particular θ_j, an increase in M_i will lead to a decrease in the shock angle ϕ_i.

The induced flow velocity behind a shock wave (Δu) depends on the flow Mach number and the shock-wave angle:

$$\Delta u_j = \frac{2}{\gamma+1}\left(M_i \sin\phi_j - \frac{1}{M_i \sin\phi_j}\right) a_i. \tag{A 7}$$

For a solution across the reflected shock set $i = 1$, $j = 2$.

Figure 32(*a*,*b*) shows the behaviour of the reflected shock-wave angle and the induced flow Mach number behind the reflected shock wave at a constant deflection angle.

REFERENCES

ANSYS® Academic Research, Release 15.0, Theory Guide, ANSYS, Inc, 2013.

BARTH, T. & JESPRESEN, D. 1989 The design and application of upwind schemes on unstructured meshes. In *27th Aerospace Sciences Meeting*, American Institute of Aeronautics and Astronautics.

BEN-DOR, G. 2007 *Shock Wave Reflection Phenomena*. Springer.

BEN-DOR, G. & TAKAYAMA, K. 1986 Application of steady shock polars to unsteady shock wave reflections. *AIAA J.* **24**, 682–684.

BRYSON, A. E. & GROSS, R. W. F. 1961 Diffraction of strong shocks by cones, cylinders, and spheres. *J. Fluid Mech.* **10** (01), 1–16.

GEVA, M., RAM, O. & SADOT, O. 2013 The non-stationary hysteresis phenomenon in shock wave reflections. *J. Fluid Mech.* **732**, R1.

HAKKAKI-FARD, A. & TIMOFEEV, E. 2012 On numerical techniques for determination of the sonic point in unsteady inviscid shock reflections. *Intl J. Aero. Innov.* **4** (1–2), 41–52.

HAN, Z. Y. 1991 Shock dynamic description of reflected shock waves. In *Proc. 18th Intl Symp. Shock Waves, Sendai, Japan*, pp. 299–304. Springer.

HAN, Z. & YIN, X. 1993 *Shock Dynamics: Fluid Mechanics and its Application*, vol. 11. Kluwer Academic.

HEILIG, W. H. 1969 Diffraction of a shock wave by a cylinder. *Phys. Fluids* **12** (5), I-154.

HOLMES, D. & CONNELL, S. 1989 Solution of the 2D Navier–Stokes equations on unstructured adaptive grids. In *9th Computational Fluid Dynamics Conference*, American Institute of Aeronautics and Astronautics.

HORNUNG, H. G., OERTEL, H. JR & SANDEMAN, R. J. 1979 Transition to Mach reflection of shock waves in steady and pseudo steady flow with and without relaxation. *J. Fluid Mech.* **90**, 541–560.

https://doi.org/10.1017/jfm.2017.835 Published online by Cambridge University Press

HRYNIEWICKI, M. K., GOTTLIEB, J. J. & GROTH, C. P. T. 2016 Transition boundary between regular and Mach reflections for a moving shock interacting with a wedge in inviscid and polytropic air. *Shock Waves* **27** (4), 523–550.

ITOH, S., OKAZAKI, N. & ITAYA, M. 1981 On the transition between regular and Mach reflection in truly non-stationary flows. *J. Fluid Mech.* **108**, 383–400.

JAMESON, A., SCHMIDT, W. & TURKEL, E. 1981 Numerical solution of the euler equations by finite volume methods schemes. In *14th Fluid and Plasma Dynamic Conference*, vol. M, pp. 1–19. American Institute of Aeronautics and Astronautics.

KLEINE, H., TIMOFEEV, E., HAKKAKI-FARD, A. & SKEWS, B. 2014 The influence of Reynolds number on the triple point trajectories at shock reflection off cylindrical surfaces. *J. Fluid Mech.* **740**, 47–60.

LI, H. D. 1988 Study of transition criteria from RR to MR in truly nonstationary flows. Thesis, Univ. of Science and Technology of China.

LOCK, G. D. & DEWEY, J. M. 1989 An experimental investigation of the sonic criterion for transition from regular to Mach reflection of weak shock waves. *Exp. Fluids* **7**, 289–292.

MILTON, B. E. 1975 Mach reflection using ray-shock theory. *AIAA J.* **13** (11), 1531–1533.

VON NEUMANN, J. 1943*a* Oblique reflection of shocks. *Explos. Res. Rep*. 12, Navy Dept., Bureau of Ordinance, Washington, DC, USA.

VON NEUMANN, J. 1943*b* Refraction, intersection and reflection of shock waves. *NAVORD Rep*. 203-45, Navy Dept., Bureau of rdinance, Washington, DC, USA.

PRATT, V. 1987 Direct least-squares fitting of algebraic surfaces. *Comput. Graph.* **21** (4), 145–152.

RAM, O., GEVA, M. & SADOT, O. 2015 High spatial and temporal resolution study of shock wave reflection over a coupled convex–concave cylindrical surface. *J. Fluid Mech.* **768**, 219–239.

RAUSCH, R. D., BATINA, J. T. & YANG, H. T. Y. 1992 Spatial adaptation of unstructured meshes for unsteady aerodynamic flow computations. *AIAA J.* **30** (5), 1243–1251.

SHIROUZU, M. & GLASS, I. I. 1986 Evaluation of assumptions and criteria in pseudostationary oblique shock-wave reflections. *Proc. R. Soc. Lond.* A **406** (1830), 75–92.

SKEWS, B. & KLEINE, H. 2009 Unsteady flow diagnostics using weak perturbations. *Exp. Fluids* **46**, 65–76.

SKEWS, B. W. & BLITTERSWIJK, A. 2011 Shock wave reflection off coupled surfaces. *Shock Waves* **21**, 491–498.

SKEWS, B. W. & KLEINE, H. 2010 Shock wave interaction with convex circular cylindrical surfaces. *J. Fluid Mech.* **654**, 195–205.

TAKAYAMA, K. & SASAKI, M. 1983 Effects of radius of curvature and initial angle on the shock transition over concave and convex walls. *Reports of the Institute of High Speed Mechanic* **46**, 1–30.

TIMOFEEV, E., SKEWS, B. W., VOINOVICH, P. A. & TAKAYAMA, K. 1999 The influence of unsteadiness and three-dimensionality on regular-to-Mach reflection transitions: a high-resolution study. In *Proc. 22nd Int. Symp. Shock Waves, Imperial College, London*, vol. 2, pp. 1231–1236. University of Southampton.

VIGNATI, F. & GUARDONE, A. 2016 Leading edge reflection patterns for cylindrical converging shock waves over convex obstacles. *Phys. Fluids* **28** (9), 096103.

WHITHAM, G. B. 1968 A note on shock dynamics relative to a moving frame. *J. Fluid Mech.* **31** (3), 449–453.

https://doi.org/10.1017/jfm.2017.835 Published online by Cambridge University Press